CHALMERS
UNIVERSITY OF TECHNOLOGY

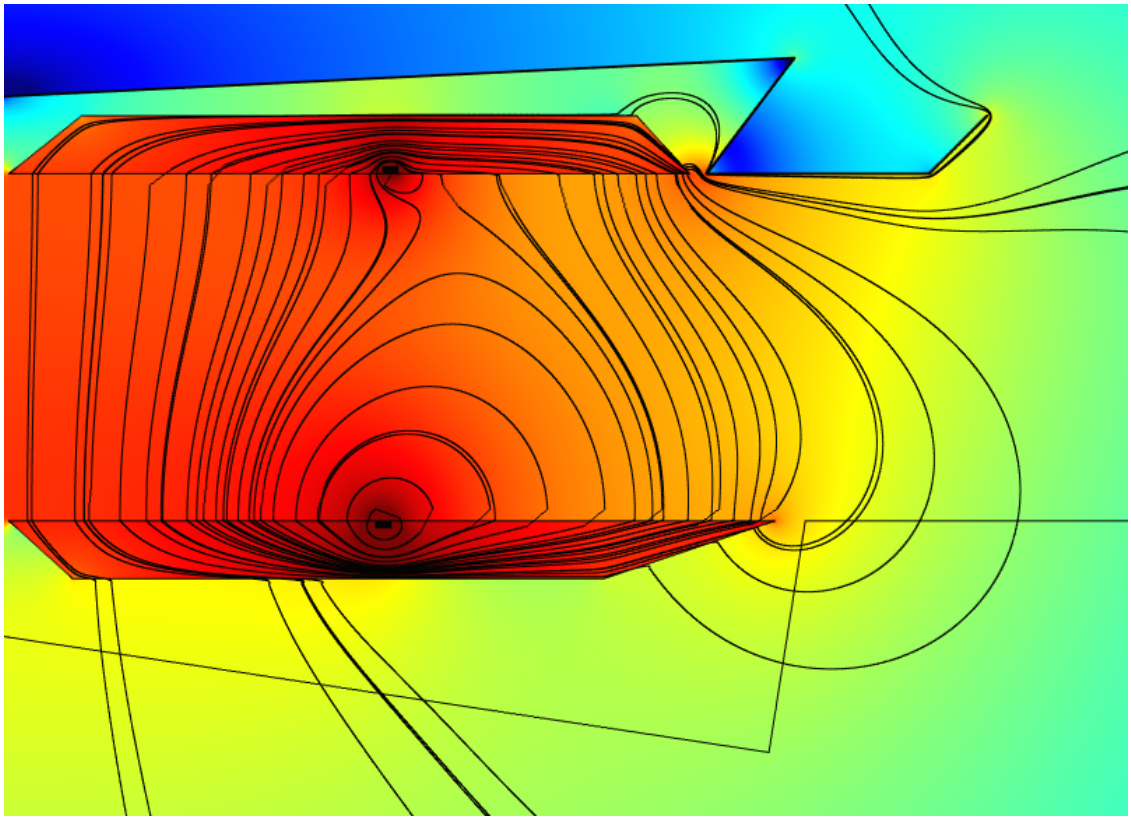

Wireless Energy Transfer by Resonant Inductive Coupling

Master of Science Thesis

Rikard Vinge

Department of Signals and systems
CHALMERS UNIVERSITY OF TECHNOLOGY
Göteborg, Sweden 2015

Master's thesis EX019/2015

Wireless Energy Transfer by Resonant Inductive Coupling

Rikard Vinge

CHALMERS
UNIVERSITY OF TECHNOLOGY

Department of Signals and systems
Division of Signal processing and biomedical engineering
Signal processing research group
Chalmers University of Technology
Göteborg, Sweden 2015

Wireless Energy Transfer by Resonant Inductive Coupling
Rikard Vinge

Main supervisor: Thomas Rylander, Department of Signals and systems
Additional supervisor: Johan Winges, Department of Signals and systems
Examiner: Thomas Rylander, Department of Signals and systems

Master's Thesis EX019/2015
Department of Signals and systems
Division of Signal processing and biomedical engineering
Signal processing research group
Chalmers University of Technology
SE-412 96 Göteborg
Telephone +46 (0)31 772 1000

Cover: Magnetic field lines between the primary and secondary coil in a wireless energy transfer system simulated in `COMSOL`.

Typeset in LaTeX
Göteborg, Sweden 2015

Wireless Energy Transfer by Resonant Inductive Coupling
Rikard Vinge
Department of Signals and systems
Chalmers University of Technology

Abstract

This thesis investigates wireless energy transfer systems based on resonant inductive coupling with applications such as charging electric vehicles. Wireless energy transfer can be used to power or charge stationary and moving objects and vehicles, and the interest in energy transfer over the air has grown considerably in recent years.

We study wireless energy transfer systems consisting of two resonant circuits that are magnetically coupled via coils. Further, we explore the use of magnetic materials and shielding metal plates to improve the performance of the energy transfer. To ensure that the wireless energy transfer systems are safe to use by the general public, we optimize our systems to maximize the transferred power and efficiency subject to the constraint that the magnetic fields that humans or animals may be exposed to are limited in accordance with international guidelines.

We find that magnetic materials can significantly increase the coupling between the two coils and reduce the induced currents and losses in the shielding metal plates. Further, we design wireless energy transfer systems capable of a peak-value power transfer of 1.3 kW with 90% efficiency over an air gap of 0.3 m. This is achieved without exceeding the exposure limit of magnetic fields in areas where humans can be present. Higher levels of transferred power is possible if larger magnetic fields are allowed.

Keywords: Wireless energy transfer, resonant inductive coupling, induction, resonant circuits, ferrite.

Acknowledgements

This thesis concludes the Master's Programme in Applied Physics at Chalmers University of Technology. The work has been conducted at the Department of Signals and systems during the spring 2015. I would like to express my sincere gratitude to all who in any way have contributed to this thesis, and in particular to the following persons:

Thomas Rylander, my supervisor and examiner, for the guidance and supervision. His dedication and knowledge has been an inspiration and an invaluable support in this work.

Johan Winges for the constant support and the valuable discussions, and for the help with the cluster computations and the parametric studies.

Johan Nohlert for the help with the finite element simulations.

Yngve Hamnerius for the introduction and interesting discussion about the biological effects of electromagnetic fields.

Rikard Vinge, Göteborg, June 2015

Abbreviations

FE	Finite Element
FEM	Finite Element Method
ICNIRP	International Commission on Non-Ionizing Radiation Protection
SAE	Society of Automotive Engineers
WETRIC	Wireless Energy Transfer by Resonant Inductive Coupling
PEC	Perfect electric conductor
rms	Root mean square

Notations

ω	Angular frequency (rad/s)
f	Frequency (Hz)
L	Inductance (H)
C	Capacitance (F)
R	Resistance (Ω)
Z	Impedance (Ω)
Q	Quality factor
k	Coupling coefficient
$\vec{E}$	Electric field (V/m)
$\vec{D}$	Electric flux density (C/m^2)
$\vec{H}$	Magnetic field (A/m)
$\vec{B}$	Magnetic flux density (T)
$\vec{A}$	Magnetic vector potential (Tm)
$\vec{J}$	Current density (A/m^2)
σ	Conductivity (S/m)
ε_0	Absolute permittivity of vacuum ($\varepsilon_0 \approx 8.8541878 \cdot 10^{-12}\,\mathrm{F/m}$)
ε_r	Relative permittivity
ε	Absolute permittivity (F/m)
μ_0	Absolute permeability of vacuum ($\mu_0 = 4\pi \cdot 10^{-7}\,\mathrm{H/m}$)
μ_r	Relative permeability
μ	Absolute permeability (H/m)
c_0	Speed of light in vacuum ($c_0 = 299792458\,\mathrm{m/s}$)
j	Imaginary unit

In this thesis, three-dimensional vector quantities are denoted with arrows, and algebraic matrices and vectors with bold letters, as shown by the examples below.

$\vec{X}$	Three-dimensional vector
$\mathbf{x}$	n-dimensional vector
$\mathbf{X}$	$n \times m$-dimensional matrix

Contents

List of Figures

List of Tables

1

Introduction

This chapter introduces the history of wireless energy transfer, the problems faced when designing such systems, as well as the objective and methodology of this thesis.

1.1 Background

In the 19th century, Nikola Tesla managed to transfer energy without wires over an air gap between two axially aligned coils using magnetic fields [18]. This achievement marks the birth of the research on and development of wireless energy transfer systems, a technology which has seen a considerable growth during the last few decades. Applications that have accelerated the development of wireless energy transfer are, among others, medical implants and mobile devices such as laptops and cell phones.

In the last few years, the electric car industry has shown an increased interest in the possibility to charge vehicles wirelessly. Wireless charging stations at parking lots could ensure that your car is charged when it is time for departure. On the regular road network, wireless charging stations could be placed at intersections or along longer stretches of road, extending the operational distance of electric cars. Other applications can benefit from advances in wireless energy transfer, e.g. electric trucks in a warehouse can operate continuously if the floor is equipped with wireless charging tracks. However, simultaneous high efficiency and high power transfer in wireless energy transfer systems has proven difficult to achieve over moderate distances in air.

Today, short-distance wireless energy transfer is either based on capacitive or inductive coupling [21]. Capacitive coupling transfers energy by strong and oscillating electric field between capacitive plates. The number of applications of capacitively coupled energy transfer is limited by low power transfer, as high power transfer requires very large fields. Inductively coupled energy transfer uses the magnetic field caused by an alternating current to transfer energy between two or more coils. The coupling of both inductively and capacitively coupled wireless energy systems, is rapidly reduced as the transfer distance is increased. Often the distance is limited to a few centimeters. Another drawback is that objects placed between the capacitive plates or coils may interact strongly with the electric or magnetic fields. This

interaction tends to decrease the efficiency, lower the amount of transferred power and increase the losses in the systems. Additionally, strong electric and magnetic fields can interact with the human body with potentially harmful effects. Therefore, the European Union has enacted guidelines on the fields strengths that human beings are allowed to be exposed to. In the case of magnetic fields with frequencies up to 100 kHz, the exposure limit is 6.25 μT root mean square (rms) [7].

A method of improving the performance of inductively coupled energy transfer for larger separation distance between the coils is to utilize resonant circuits for both the primary and secondary side of the wireless power transfer system. A resonant inductive coupling energy transfer system is typically designed such that it features a few resonances. We can exploit these resonance frequencies in combination with the frequency of operation, i.e. the frequency of the applied voltage, equal to the resonance frequency of the system. This allows for the transfer of more power at higher efficiency and over longer distances than non-resonating systems. One challenge associated with resonant inductive coupling is the high sensitivity of the frequency of operation in relation to narrow frequency-bands of the wireless transfer system and its resonance frequencies, which also may drift during operation. If the energy transfer system resonates at a frequency even slightly different from the frequency of operation, the amount of transferred power and the efficiency can be reduced significantly.

In this thesis, we study wireless energy transfer systems based on resonant inductive coupling. The systems consist of two circuits, the first located in the ground, referred to as the primary side of the wireless transfer system, and the second located above ground, referred to as the secondary side. The system is inductively coupled via coils and it also contains capacitors, which we use to tune the performance of the energy transfer system.

1.2 Objective

This thesis addresses three important parts of resonant inductive energy transfer. First, circuit models are studied to gain knowledge on how the circuit component parameters influence the efficiency and magnitude of the power transfer. In the circuit models, the applied voltages and currents are assumed to be time harmonic. Next, the coil geometry is used in a field model to compute the magnetic field and its associated induced currents and voltages in the frequency domain. The coils are approximated by two-dimensional axisymmetric models and the hysteresis in ferromagnetic material is neglected. Finally, a wireless energy transfer system is optimized by means of a gradient-based method, where the design parameters describe the geometry and circuit components. Design suggestions for different situations are also given. Performance-wise, the goal is to transfer a few kW of power over an air gap of 0.3 m with high efficiency, where we attempt to limit the magnetic field strength in regions where human beings may be present.

1.3 Methodology

In this thesis, the study of wireless energy transfer using resonant inductive coupling is conducted in three steps: (i) the electrical circuits; (ii) the coil geometries; and (iii) optimization of the coil geometry and circuit components. The circuits are studied by nodal analysis, where the problem is solved both analytically and numerically. The studies are based on previous work within the area of wireless energy transfer circuit theory and reflected load theory. The coil design is studied for the case of axisymmetric geometry. Initially, Biot-Savart's law is used to analyze coils in free space in `MATLAB` [19] by computing the self and mutual inductance. The effects of different geometrical parameters, such as the number of coil winding and coil radius, are investigated. Next, a coil model including ferromagnetic materials, metals and ground is created. This model is simulated by means of the Finite Element Method (FEM) using `COMSOL` [3]. Finally, the wireless energy transfer system is optimized with respect to coil geometry and circuit components using gradient-based algorithms in `TOMLAB` [20], a `MATLAB` toolbox for solving optimization problems. The optimization is carried out in two steps. In the first step, we optimize the coil geometry to maximize the magnetic coupling between the coils. In the second step, we optimize the circuit parameters of the wireless energy transfer system to maximize the efficiency and power transfer.

2

A theoretical system model

This chapter describes the theory on which the work of this thesis is based. First, the electric circuits used to transfer power are analyzed using circuit theory. Next, the electromagnetic theory behind induction is reviewed and analytical formulas for the inductances based on integration of the magnetic vector potential are presented.

2.1 Wireless energy transfer system circuit

The circuit used for the energy transfer system in this thesis contains a capacitor, C_1, in series with the coil on the primary side and a capacitor C_2 in parallel to the coil on the secondary side. A diagram of the circuit is shown in Fig. 2.1. The voltage

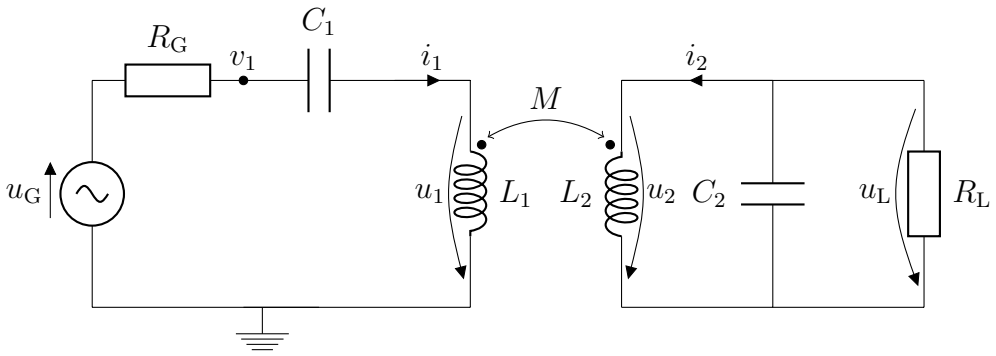

Figure 2.1: Circuit diagram with capacitor C_1 in series with the coil on the primary side. A voltage u_G is applied to the primary circuit on the left, inducing a voltage u_L in the secondary circuit on the right.

u_G is supplied by a power generator with resistance R_G. The energy is transferred between the two circuits over an air gap via the inductive coupling of the two coils, with self-inductance L_1 and L_2 and mutual inductance M. The two circuits are inductively coupled with the coupling coefficient

$$k = \frac{M}{\sqrt{L_1 L_2}}. \tag{2.1}$$

The two capacitors, C_1 and C_2, are included in the circuits to control the performance of the energy transfer system. The load-resistance R_L represents the battery we

want to charge. We can describe the circuit in Fig. 2.1 with Kirchhoff's voltage and current law

$$u_{\mathrm{G}} - R_{\mathrm{G}} i_1 - \frac{i_1}{j\omega C_1} - u_1 = 0,$$
$$i_2 + j\omega C_2 u_2 + \frac{u_2}{R_{\mathrm{L}}} = 0,$$

where u_1 and u_2 are related to i_1 and i_2 by Faraday's law

$$\begin{aligned} u_1 &= j\omega L_1 i_1 + j\omega M i_2, \\ u_2 &= j\omega M i_1 + j\omega L_2 i_2. \end{aligned} \tag{2.2}$$

In Appendix A.1, we study how the power delivered to the load R_{L} depends on the circuit components in Fig. 2.1. In Appendix A.2, we derive an expression for the maximum efficiency of the power transfer, where it is assumed that the resonance frequencies of the primary and secondary circuits are equal and identical to the frequency of operation of the wireless energy transfer system. The maximum efficiency increases monotonically with k. These results indicate that it is useful to maximize the coupling coefficient to achieve simultaneous high power and high transfer efficiency.

2.1.1 Resonant circuits

A basic building block of a resonant wireless energy transfer system is the resonant circuit. A simple resonating circuit consists of a resistor R, an inductor L and a capacitor C, connected either in series or in parallel, as shown in Fig. 2.2. In a

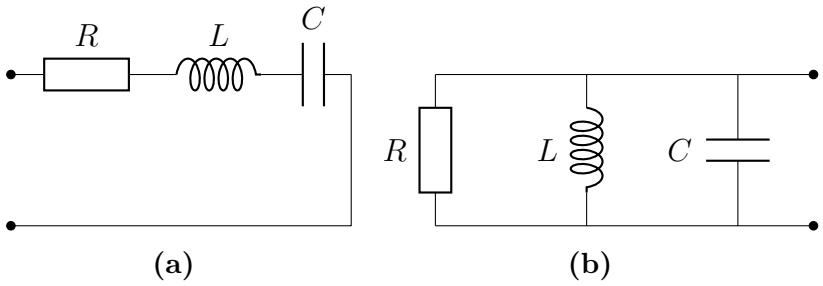

Figure 2.2: (a) Series and (b) parallel RLC circuit.

frequency interval around $\omega_0 = (LC)^{-1/2}$ the energy in the resonant circuit oscillates between electric energy stored in the capacitor and magnetic energy stored in the inductor. The losses in the resonator are due to resistance R.

2.1.1.1 Quality factor and bandwidth

Currents and charges in the resonating circuit stores energy in electric and magnetic fields. This stored energy is dissipated by Ohmic and radiative losses. The quality

factor, or Q-factor, of a circuit with resonance frequency ω_0 is defined as

$$Q = \omega_0 \frac{W}{P} = 2\pi \frac{\text{stored electric and magnetic energy}}{\text{energy dissipated during one period}},$$

where W is the total energy stored in the resonator by the electric and magnetic fields and P is the resistive power loss during one period. A high Q-factor implies that the circuit can store a large amount of energy in comparison to the energy dissipated during one period. For the resonance frequency ω_0, the quality factor can be expressed as

$$Q = \begin{cases} \frac{\omega_0 L}{R}, & \text{series resonating circuit} \\ \frac{R}{\omega_0 L}, & \text{parallel resonating circuit} \end{cases}$$

The bandwidth of a resonant circuit is

$$\text{BW} = \frac{\omega_0}{Q}.$$

This implies that a high Q-resonator also has a narrow bandwidth, and the frequency range of resonant behavior of the circuit is limited.

2.1.1.2 Coupled resonators

When isolated from each other, i.e. $k = 0$, the resonance frequencies of the primary and secondary resonance circuits in Fig. 2.1 are

$$\omega_1 = \frac{1}{\sqrt{C_1 L_1}} \quad \text{and} \quad \omega_2 = \frac{1}{\sqrt{C_2 L_2}}. \tag{2.3}$$

However, $k > 0$ implies that the two resonators are magnetically coupled to each other and can exchange energy. The two circuits become a single circuit with resonance frequencies that deviate from ω_1 and ω_2. For $R_\text{L} \to \infty$, the input impedance of the circuit in Fig. 2.1 is

$$Z_\text{in} = \frac{v_1}{i_1} = \frac{\left(j\omega L_1 + \frac{1}{j\omega C_1}\right)\left(j\omega L_2 + \frac{1}{j\omega C_2}\right) + \omega^2 M^2}{j\omega L_2 + \frac{1}{j\omega C_2}}. \tag{2.4}$$

At resonance, the reactance of the circuit is zero, i.e. $\Im\left(Z_\text{in}\right) = 0$. Next, we use Eq. (2.4) and solve $\Im\left(Z_\text{in}\right) = 0$ to find the resonance frequencies ω_sys of the magnetically coupled system. The result is a fourth degree polynomial with the solutions

$$\omega_\text{sys} = \pm \frac{1}{\sqrt{2}} \sqrt{\frac{\omega_1^2 + \omega_2^2 \pm \sqrt{\left(\omega_1^2 + \omega_2^2\right)^2 - 4\omega_1^2 \omega_2^2 \left(1 - k^2\right)}}{1 - k^2}}, \tag{2.5}$$

when expressed in terms of Eq. (2.1) and Eq. (2.3). The interesting system resonance frequencies are positive and thus we can discard two of the solutions in Eq. (2.5). If the capacitors are chosen such that $\omega_1 = \omega_2 = \omega_0$, the coupled circuit resonates at

$$\omega_\text{sys} = \frac{\omega_0}{\sqrt{1 \pm k}}. \tag{2.6}$$

It is clear that as the coupling coefficient k increases, the resonance frequencies of the coupled circuit are shifted away from the resonant frequencies of the individual resonance circuits.

2.1.2 Circuit components

In this section, we model the circuit components of the wireless power transfer system for a class of physical situations that allow for analytical treatment.

2.1.2.1 Inductance for simple coil geometries

One objective in the design problem in this thesis is to compute the magnetic fields due to currents flowing in coils. If the physical size of the system and its components is much smaller than the wavelength associated with the exciting current, the magnetic field $\vec{H}$ can be found from the quasi-magnetostatic Ampère's law of induction

$$\nabla \times \vec{H} = \vec{J},$$

where $\vec{J}$ is the current density. It is convenient to formulate the problem in terms of the magnetic vector potential $\vec{A}$ instead of the magnetic field, using the relation

$$\vec{A} = \nabla \times \vec{B}.$$

Ampère's law for the magnetic vector potential for problems with permeability μ is then formulated as

$$\nabla \times \left(\mu^{-1} \nabla \times \vec{A}\right) = \vec{J}. \tag{2.7}$$

One method to solve Eq. (2.7) is to use the FEM, which is a computational method for solving partial differential equations. With the FEM, the magnetic fields can be solved for complex geometries and material properties. For sufficiently simple problems, Eq. (2.7) can be solved analytically, using e.g. Biot-Savart's law [2].

From the magnetic flux density, we can calculate the magnetic flux through a surface S and surface normal $\hat{n}$ as

$$\Phi = \iint_S \vec{B} \cdot \hat{n}\, ds. \tag{2.8}$$

If a current I_1 flows through a coil 1, the self-inductance of coil 1 and the mutual inductance of an coil 2 is defined as

$$\begin{aligned} L_1 = L_{11} &= \frac{\Phi_{11}}{I_1}, \\ M = L_{21} &= \frac{\Phi_{21}}{I_1}, \end{aligned} \tag{2.9}$$

where Φ_{11} and Φ_{21} are the magnetic flux through coil 1 and 2, respectively, due to the current flowing in coil 1.

The self-inductance for a single, circular wire loop in vacuum, as shown in Fig. 2.3(a), can be expressed analytically [8] as

$$L = \mu_0 a \left(\ln\left(\frac{8a}{r}\right) - 2\right), \tag{2.10}$$

if the current is confined to the surface of the wire, and

$$L = \mu_0 a \left(\ln \left(\frac{8a}{r} \right) - \frac{7}{4} \right), \tag{2.11}$$

if the current density is uniform over the wire cross section. The analytical expression

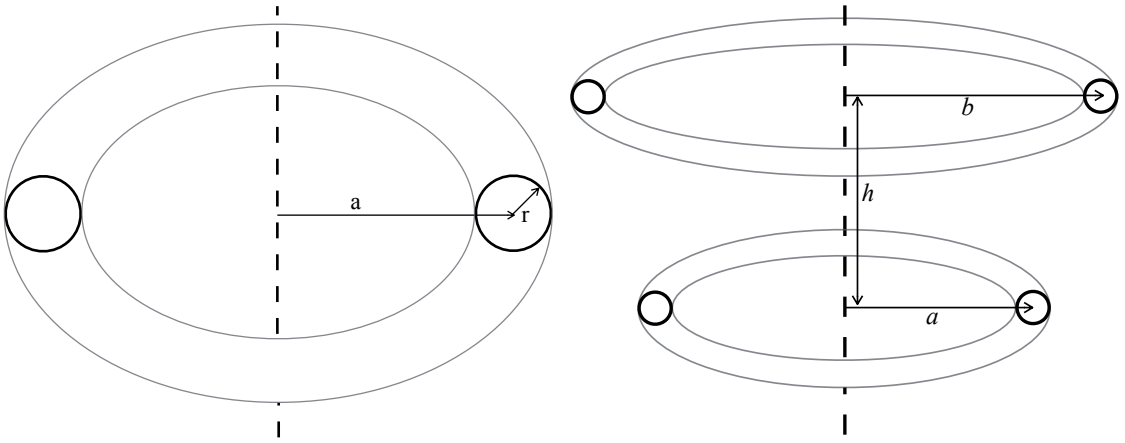

Figure 2.3: (a) Single conductive wire loop of loop radius a and wire radius r. (b) Two axially aligned wire loops of loop radius a and b respectively and separated a distance h.

for the mutual inductance between two thin, circular and coaxial wire loops in free space, as shown in Fig. 2.3(b), is

$$M = \mu_0 \sqrt{ab} m^{3/2} C(m) = \mu_0 \sqrt{ab} \left[\left(\frac{2}{\sqrt{m}} - \sqrt{m} \right) K(m) - \frac{2}{\sqrt{m}} E(m) \right], \tag{2.12}$$

where a and b are the radii of the two wire loops and

$$m = \frac{4ab}{(a+b)^2 + h^2},$$

where h is the distance between the loop centers. The functions $C(m)$, $K(m)$ and $E(m)$ are the complete elliptic integrals.

For a coil with N turns of a thin wire, we get rather simple expressions for the inductances if all turns coincide with the same circular loop. If two such coils are placed coaxially, the self- and mutual inductance become

$$\begin{aligned} L_1 &= N_1^2 \mu_0 a \left(\ln \left(\frac{8a}{r_1} \right) - 2 \right), \\ L_2 &= N_2^2 \mu_0 b \left(\ln \left(\frac{8b}{r_2} \right) - 2 \right), \\ M &= N_1 N_2 \mu_0 \sqrt{ab} m^{3/2} C(m), \end{aligned} \tag{2.13}$$

where the wire radius of coil 1 and 2 is r_1 and r_2, respectively. The number of turns is N_1 and N_2 for coil 1 and 2, respectively. The radius of coil 1 is a and the radius of coil 2 is b.

A more realistic model of an axisymmetric coil is to take the N single-turn wire loops and use their actual locations as they are distributed in space. The mutual inductance between two such coils is the sum of the contribution from all loops in one coil to all loops in the other,

$$M = \sum_{i=1}^{N_1}\sum_{j=1}^{N_2} M_{ij} = \sum_{i=1}^{N_1}\sum_{j=1}^{N_2} \mu_0\sqrt{a_i b_j} m_{ij}^{3/2} C(m_{ij}), \tag{2.14}$$

where $i = 1, 2, ...N_1$, $j = 1, 2, ...N_2$, a_i (b_j) the radius of loop i (j) of the first (second) coil and

$$m_{ij} = \frac{4a_i b_j}{(a_i + b_j)^2 + h_{ij}^2}.$$

The self-inductance of a coil with N windings with wire radius r_i, loop radius a_i and an axial distance between winding i and j of h_{ij}, where $i = 1, 2, ..., N$ and $j = 1, ..., i-1, i+1, ...N$ is

$$L = \sum_{i=1}^{N}\left(\mu_0 a_i\left(\ln\left(\frac{8a_i}{r_i}\right) - 2\right) + \sum_{\substack{j=1\\ j\neq i}}^{N} \mu_0\sqrt{a_i a_j} m_{ij}^{3/2} C(m_{ij})\right), \tag{2.15}$$

where m_{ij} is here defined as

$$m_{ij} = \frac{4a_i a_j}{(a_i + a_j)^2 + h_{ij}^2}.$$

Note that Eq. (2.15) assumes that the current is confined to the surface of the wires. If the current flows uniformly through the whole cross section of the wires, the expression for the self-inductance in Eq. (2.11) should be used, i.e. the constant 2 is replaced by 7/4. We see from Eq. (2.15) that the contribution from winding i comes from the self-inductance of winding i and the mutual inductance between winding i and all remaining windings. If N is large, the mutual inductance contribution can become dominant.

2.1.2.2 Coil resistance

A simple circuit model of a resistive coil is an ideal inductor connected in series with a resistor, as shown in Fig. 2.4.

The resistance of the coil wire can be calculated if the material properties and frequency of operation is known. The skin depth [8] can be used to approximately describe how an alternating current penetrates into a solid conductor and it is defined as

$$\delta = \sqrt{\frac{2}{\mu\sigma\omega}}. \tag{2.16}$$

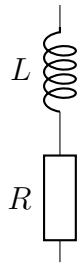

Figure 2.4: Circuit model of a coil with wire resistance R and inductance L.

Copper has the relative permeability $\mu_\mathrm{r} \approx 1$ and conductivity $\sigma = 5.80 \cdot 10^7\,\mathrm{S/m}$ [2], which yields the skin depth 0.2 mm at a frequency of 100 kHz. For a conductor shaped as a cylinder of circular cross section with length L and radius r, the resistance can easily be estimated in two important extreme cases

$$R = \begin{cases} \frac{L}{\sigma\pi r^2}, & r \ll \delta, \\ \frac{L}{2\pi\sigma r\delta}, & r \gg \delta. \end{cases} \tag{2.17}$$

Thus, solid wires with $r \gg \delta$ have significantly higher as compared to wires with $r \ll \delta$ for alternating currents.

Another drawback of solid wires is the so-called proximity effects, i.e. nearby wires induces currents that further increases the resistance of the coil [17]. An attractive alternative to the solid wire is the so-called litz wire, which is manufactured from thin, insulated wire strands that are woven together into a braid. The dimensions of the strands are chosen such that their radius is much smaller than the skin depth, in order to ensure that current flows through the full cross section of the strands. This makes the resistance of the litz wire relatively small and approximately constant for frequencies below the frequency where the skin depth is comparable to the strand radius. A litz wire braid features some insulation and air between the strands and, thus, the effective area of the litz wire is less than about 0.9 times the braid area [5].

2.1.2.3 Self-resonant coils

At low frequency, it is sufficient to model a coil as an ideal inductor in series with a resistance, while the behavior at higher frequencies can be significantly different. Assuming a time-harmonic current excitation, a coil becomes self-resonant when its wire length is approximately equal to half the wavelength in free-space at the excitation frequency. A simplistic model of this behavior is to connect a parasitic capacitor in parallel to the inductor and resistance [12], see Fig. 2.5. This self-resonance can be exploited in wireless energy transmission. In Ref. [10], for example, an efficiency of 40% is achieved over a distance of 2 m using self-resonant coils. However, the analysis of such a system requires the solution of the complete Maxwell's equations, whereas this thesis is focused on quasi-magnetostatic realizations of wireless power-transfer systems. Thus, we limit the length of the coil wires such that the self-resonance of the coils occur at significantly higher frequencies than that of the frequency of

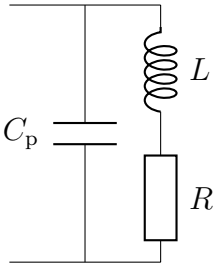

Figure 2.5: Circuit model of a self-resonant coil with wire resistance R, inductance L and a parasitic capacitance C_p.

operation. The length limitation is related to the self-resonance frequency ω_r, as

$$\omega_\mathrm{r} \approx \frac{\pi c}{l} = \frac{\pi c_0}{l\sqrt{\varepsilon_\mathrm{r}\mu_\mathrm{r}}},$$

where c is the speed of light in the surrounding medium, c_0 the speed of light in vacuum and l the wire length. A coil with self-inductance L resonates at

$$\omega_\mathrm{r}^2 = \frac{1}{LC_\mathrm{p}} = \left(\frac{\pi c_0}{l\sqrt{\varepsilon_\mathrm{r}\mu_\mathrm{r}}}\right)^2,$$

where C_p is the parasitic capacitance of the coil. The coils should behave inductive at the frequency of operation. Thus, at the frequency of operation ω_0, the following relation must be satisfied

$$\frac{1}{\omega_0 C_\mathrm{p}} \gg \omega_0 L.$$

We rewrite this expression to find a constraint for the wire length,

$$l^2 \ll \left(\frac{\pi c_0}{\omega_0\sqrt{\varepsilon_\mathrm{r}\mu_\mathrm{r}}}\right)^2.$$

This is equivalent to the equation

$$\xi l^2 = \left(\frac{\pi c_0}{\omega_0\sqrt{\varepsilon_\mathrm{r}\mu_\mathrm{r}}}\right)^2, \quad \text{where} \quad \xi \gg 1.$$

Thus, the wire length is constrained by

$$l < \frac{\pi c_0}{\omega_0\sqrt{\xi\varepsilon_\mathrm{r}\mu_\mathrm{r}}}. \tag{2.18}$$

The value of the parameter ξ should be at least 10 for the coil to be mainly inductive at ω_0.

If we wind the coil wire around a material with high permeability μ_r, the effective permeability for the coils is increased compared to the permeability of air. The exact value of the effective permeability is difficult to determine, and we approximate an effective relative permeability as

$$\mu_\mathrm{r}^\mathrm{eff} \approx \frac{\mu_\mathrm{r} + 1}{2}$$

for a situation with the material with high permeability on one side of the coil and air on the other side as shown in Fig. 2.7(a).

2.1.2.4 Load resistance

The load-resistance R_{L} in the power transfer system circuit represents the battery being charged. The impedance of a real battery varies during a charging cycle [1]. A good charging system should therefore be able to handle varying load-resistances. A battery has a low internal resistance to reduce the dissipated heat in the battery as it delivers a current to an external load, such as the motor in an electric vehicle.

Using reflected load theory and assuming that the two resonating circuits are set to individually resonate at $\omega_1 = \omega_2 = \omega_0$, where ω_0 is the frequency of operation, we can prove that the efficiency of the energy transfer maximizes if the load-resistance is chosen according to

$$R_{\mathrm{L}}^{\mathrm{opt}} = R_2 \frac{Q_2^2}{\sqrt{1 + k^2 Q_1 Q_2}}. \tag{2.19}$$

where Q_1 and Q_2 are the quality factors of the two resonators. Equation (2.19) is derived in Appendix A.2. For $Q_1 \approx Q_2 \gg k$ the expression for the optimal load-resistance simplifies to

$$R_{\mathrm{L}}^{\mathrm{opt}} \approx \frac{\omega L_2}{k}. \tag{2.20}$$

In Eq. (2.20), L_2 and k are characteristics of the coils and these are difficult to change after the wireless energy transfer system has been manufactured. We can, however, change the frequency of operation if the capacitors C_1 and C_2 are variable. With control over the frequency and the capacitors, the resonance peak can be shifted in frequency and an optimal load-resistance achieved for a broader set of frequencies than a system working at a single frequency.

2.1.2.5 Model of the generator resistance

This section describes a potential power source for the wireless energy transfer system, utilizing a rectifying and switching network to convert the 50 Hz power grid AC to the frequency of operation of the energy transfer system. Other power sources are possible and the main result of this section is to estimate the generator resistance.

A simple example of a power source is a rectifier (four diodes) and switching network (four power MOSFET transistors), as shown in Fig. 2.6. The resistance of this network is, approximately, that of two of the diodes and two of the transistors in series. Typical values for the drain-source resistance of a power MOSFET transistor is in the range of 25 mΩ to 100 mΩ when it conducts a current from the source to the drain. The corresponding resistance of a diode is approximately 100 mΩ. Thus, the resistance of this power source is in the range of 250 mΩ to 400 mΩ.

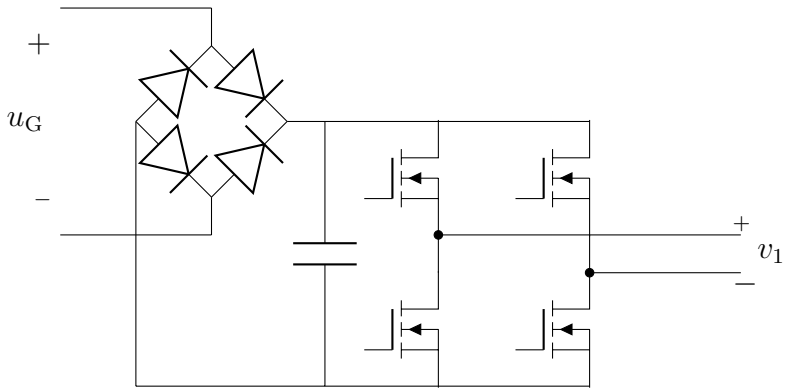

Figure 2.6: Circuit diagram of a simple power generator that converts 50 Hz grid AC to kHz.

2.1.2.6 Higher frequency components

The output from the switching network in Section 2.1.2.5 is approximately a square voltage. The Fourier components of a normalized square signal $f(t)$ is

$$f(t) = \frac{4}{\pi} \sum_{n=1,3,5,\ldots}^{\infty} \frac{1}{n} \sin\left(\frac{2n\pi t}{T}\right), \tag{2.21}$$

where T is the period of the signal. From Eq. (2.21), it is given that the first overtone is located at three times the frequency of the fundamental frequency. For a frequency of operation of 85 kHz and a resonator quality factor of 100 this means that the bandwidth is less than 10 kHz from the center peak. The first overtone has a frequency of 255 kHz, i.e. basically no energy of the overtones is stored in the resonator. Thus, the fundamental frequency is dominant in a wireless power transfer system with reasonably high Q-values.

2.2 Numerical modelling with the FEM

Problems that include conductive, dielectric and magnetic materials and complicated geometries require more sophisticated tools than Biot-Savart's law. Instead, we use the full Ampère's law, which we express in terms of the magnetic vector potential as

$$\nabla \times \left(\mu^{-1} \nabla \times \vec{A}\right) = \frac{\partial \vec{D}}{\partial t} + \vec{J},$$

where $\vec{D}$ is the electric displacement field. Faraday's law gives

$$\nabla \times \vec{E} = -\frac{\partial}{\partial t}\left(\nabla \times \vec{A}\right),$$

which allows for the introduction of the curl-free quantity $\nabla\phi$ as

$$\nabla \times \left(\vec{E} + \frac{\partial \vec{A}}{\partial t}\right) = \nabla \times (-\nabla\phi) = 0.$$

The total current density $\vec{J}$ is the combined eddy current density and a source current density $\vec{J}_{\mathrm{e}}$. Thus, we have

$$\begin{aligned} \vec{J} &= \sigma\vec{E} + \vec{J}_{\mathrm{e}}, \\ \vec{D} &= \varepsilon\vec{E}, \end{aligned} \tag{2.22}$$

and

$$\vec{E} = -\nabla\phi - \frac{\partial\vec{A}}{\partial t}, \tag{2.23}$$

where σ is the conductivity and ε is the permittivity. The axisymmetric problem with $\vec{A} = \hat{\varphi}A_{\varphi}(r,z)$ automatically yields $\nabla\cdot\vec{A} = 0$ and we set $\phi = 0$. This allows us to to write the current density and electric displacement field as

$$\begin{aligned} \vec{J} &= -\sigma\frac{\partial\vec{A}}{\partial t} + \vec{J}_{\mathrm{e}}, \\ \vec{D} &= -\varepsilon\frac{\partial\vec{A}}{\partial t}. \end{aligned} \tag{2.24}$$

Next, we combine Eq. (2.22), Eq. (2.23) and Eq. (2.24) with Ampère's law and find

$$\sigma\frac{\partial\vec{A}}{\partial t} + \varepsilon\frac{\partial^2\vec{A}}{\partial^2 t} + \nabla\times\left(\mu^{-1}\nabla\times\vec{A}\right) = \vec{J}_{\mathrm{e}} \tag{2.25}$$

In frequency-domain studies, we work with time-harmonic quantities and this enables us to write Eq. (2.25) as

$$\left(j\omega\sigma - \omega^2\varepsilon\right)\vec{A} + \nabla\times\left(\mu^{-1}\nabla\times\vec{A}\right) = \vec{J}_{\mathrm{e}}. \tag{2.26}$$

We can solve Eq. (2.26) with boundary conditions for complicated geometries with conductive, dielectric and magnetic materials by means of the FEM. From the solution to Eq. (2.26), we can calculate the currents and voltages everywhere in the problem geometry. Thus we can calculate the voltages induced over the coils due to current excitations in the coils. The coil model can no longer be fully described by only the self- and mutual inductance and coil resistance, but must be described by the full impedance matrix

$$\mathbf{Z} = \begin{bmatrix} Z_{11} & Z_{12} \\ Z_{21} & Z_{22} \end{bmatrix} = \begin{bmatrix} R_{11} + j\omega L_{11} & R_{12} + j\omega L_{12} \\ R_{21} + j\omega L_{21} & R_{22} + j\omega L_{22} \end{bmatrix}, \tag{2.27}$$

where R_{11} and R_{22} are the self-resistances, L_{11} and L_{22} are the self-inductances and L_{12} and L_{21} the mutual inductances as before. The quantities R_{12} and R_{21} are called the mutual resistance. Due to reciprocity of the problem we have $Z_{12} = Z_{21}$. In the following, the simplified notation for the resistances and inductances in Tab. 2.1 is used.

The voltages over the coils, i.e. u_1 and u_2 in Fig. 2.1, can be related to the currents flowing through them via the impedance matrix $\mathbf{Z}$ as

$$\begin{aligned} \mathbf{u} &= \mathbf{Z}\mathbf{i}, \\ &\Updownarrow \\ \begin{bmatrix} u_1 \\ u_2 \end{bmatrix} &= \begin{bmatrix} Z_{11} & Z_{12} \\ Z_{12} & Z_{22} \end{bmatrix}\begin{bmatrix} i_1 \\ i_2 \end{bmatrix}. \end{aligned} \tag{2.28}$$

Table 2.1: Notation used for the self- and mutual resistance and inductance for the energy transfer system consisting of the coils and surrounding objects.

	Notation in Eq. (2.27)	New notation
Self-resistance	R_{11} and R_{22}	R_1 and R_2
Mutual resistance	R_{12} and R_{21}	R_{12}
Self-inductance	L_{11} and L_{22}	L_1 and L_2
Mutual inductance	L_{12} and L_{21}	M

The elements of the impedance matrix is found by the following procedure. If we force the current through the secondary coil to be zero, i.e. $i_2 = 0$, we find

$$\begin{aligned} u_1 &= Z_{11} i_1, \\ u_2 &= Z_{21} i_1. \end{aligned} \tag{2.29}$$

Given an imposed current i_1, we compute the induced voltages u_1 and u_2 by the FEM. Finally, we get $Z_{11} = u_1/i_1$ and $Z_{21} = u_2/i_1$. Similarly, if we force the current through the primary coil to be zero, we find

$$\begin{aligned} u_1 &= Z_{12} i_2, \\ u_2 &= Z_{22} i_2. \end{aligned} \tag{2.30}$$

Now, we get $Z_{12} = u_1/i_2$ and $Z_{22} = u_2/i_2$.

We use Eq. (2.28) to calculate the power dissipated in the coils. The complex power is defined as

$$S = \mathbf{u}^{\mathrm{T}} \mathbf{i}^* = (\mathbf{Z}\mathbf{i})^{\mathrm{T}} \mathbf{i}^* = \mathbf{i}^{\mathrm{T}} \mathbf{Z}^{\mathrm{T}} \mathbf{i}^*,$$

where the complex current is

$$\mathbf{i} = \begin{bmatrix} i_1^{\mathrm{R}} + j i_1^{\mathrm{I}} \\ i_2^{\mathrm{R}} + j i_2^{\mathrm{I}} \end{bmatrix}.$$

This gives us the net complex power delivered to the transformer represented by Eq. (2.28) as

$$S = \mathbf{i}^{\mathrm{T}} \mathbf{Z}^{\mathrm{T}} \mathbf{i}^* = \begin{bmatrix} Z_{11}(i_1^{\mathrm{R}} + j i_1^{\mathrm{I}}) + Z_{12}(i_2^{\mathrm{R}} + j i_2^{\mathrm{I}}) \\ Z_{21}(i_1^{\mathrm{R}} + j i_1^{\mathrm{I}}) + Z_{22}(i_2^{\mathrm{R}} + j i_2^{\mathrm{I}}) \end{bmatrix}^{\mathrm{T}} \begin{bmatrix} i_1^{\mathrm{R}} - j i_1^{\mathrm{I}} \\ i_2^{\mathrm{R}} - j i_2^{\mathrm{I}} \end{bmatrix} =$$

$$= Z_{11}|i_1|^2 + Z_{22}|i_2|^2 + Z_{12}\left(i_1^{\mathrm{R}} i_2^{\mathrm{R}} + i_1^{\mathrm{I}} i_2^{\mathrm{I}} + j\left(i_1^{\mathrm{R}} i_2^{\mathrm{I}} - i_2^{\mathrm{R}} i_1^{\mathrm{I}}\right)\right) +$$

$$+ Z_{21}\left(i_1^{\mathrm{R}} i_2^{\mathrm{R}} + i_1^{\mathrm{I}} i_2^{\mathrm{I}} + j\left(i_2^{\mathrm{R}} i_1^{\mathrm{I}} - i_1^{\mathrm{R}} i_2^{\mathrm{I}}\right)\right).$$

The resistive losses correspond to the real part of the complex power. Thus, the resistive losses are

$$P = \Re(S) = R_{11}|i_1|^2 + 2R_{12}\left(i_1^{\mathrm{R}} i_2^{\mathrm{R}} + i_1^{\mathrm{I}} i_2^{\mathrm{I}}\right) + R_{22}|i_2|^2, \tag{2.31}$$

and we find that it is desirable to reduce the self-and mutual resistances in order to achieve a transformer with low losses.

We validate the FEM models with analytical formulas and extrapolate the results from the FEM computations in Appendix B.

2.2.1 Effects of nearby conductive and magnetic materials

The magnetic field at the interface between medium 1 and medium 2 satisfies the boundary conditions

$$\hat{n} \cdot \left(\mu_1 \vec{H}_1 - \mu_2 \vec{H}_2\right) = 0, \tag{2.32}$$

$$\hat{n} \times \left(\vec{H}_1 - \vec{H}_2\right) = \vec{J}_\mathrm{s}, \tag{2.33}$$

where $\vec{H}_1$ and $\vec{H}_2$ are the magnetic fields in medium 1 and 2, respectively. Further, $\hat{n}$ is the surface normal of the interface that points away from medium 2. In Eq. (2.32), μ_1 denotes the permeability of medium 1 and μ_2 denotes the permeability of medium 2.

At high frequencies, we often approximate metals as perfect electrical conductors (PECs), i.e. the skin depth $\delta \to 0$. There are no electric or magnetic fields in the interior of a PEC for $\omega = 0$ [2]. For such a situation, the normal boundary condition in Eq. (2.32) gives that the normal component of the magnetic field is zero at the interface to a PEC. Further, if medium 2 is a PEC, the surface current density on the surface of medium 2 is described by

$$\vec{J}_\mathrm{s} = \hat{n} \times \vec{H}_1.$$

At the interface between two magnetic materials with permeability μ_1 and μ_2, the (quasi-) static magnetic field may rapidly change direction. We assume that the magnetic field in medium 1 has the magnitude H_1 and it makes an angle α_1 to the normal $\hat{n}$. Similarly, the angle α_2 and the magnitude H_2 of the magnetic field in medium 2 yields the boundary conditions

$$\mu_1 H_1 \cos\alpha_1 = \mu_2 H_2 \cos\alpha_2,$$
$$H_1 \sin\alpha_1 = H_2 \sin\alpha_2,$$

which gives the direction of the magnetic field in medium 2 as

$$\alpha_2 = \tan^{-1}\left(\frac{\mu_2}{\mu_1}\tan\alpha_1\right).$$

Thus, we consider a situation where the permeability of medium 1 is much larger than the permeability of medium 2. Then, the magnetic field at the interface in medium 2 is almost perpendicular to the interface, regardless of α_1. A nonconductive and ferromagnetic material often used in transformer applications is ferrite [14]. Ferrites can be manufactured by mixing iron powder into ceramic materials and they can have relative permeabilities up to the order of several tens of thousands [6, 13].

2.2.2 Reluctance of a wireless energy transfer system

The magnetic induction system shown in Fig. 2.7(a) can be thought of as a magnetic circuit, similar to an electric circuit. Figure 2.7(b) shows a magnetic circuit where the magnetomotive force Ni yields a magnetic flux Φ through the reluctance $\mathcal{R}$ according to

$$Ni = \mathcal{R}\Phi.$$

We estimate the reluctance of a simple energy transfer system shown in Fig. 2.7. The system consists of two coaxial coils of equal radius b, which are placed a distance d apart. The system is equipped with two ferrite plates of circular shape with a hole at the center. These annulus plates have thickness h, inner radius a, outer radius c, and relative permeability μ_r. Below, we assume that $a < b < c$. We assume that

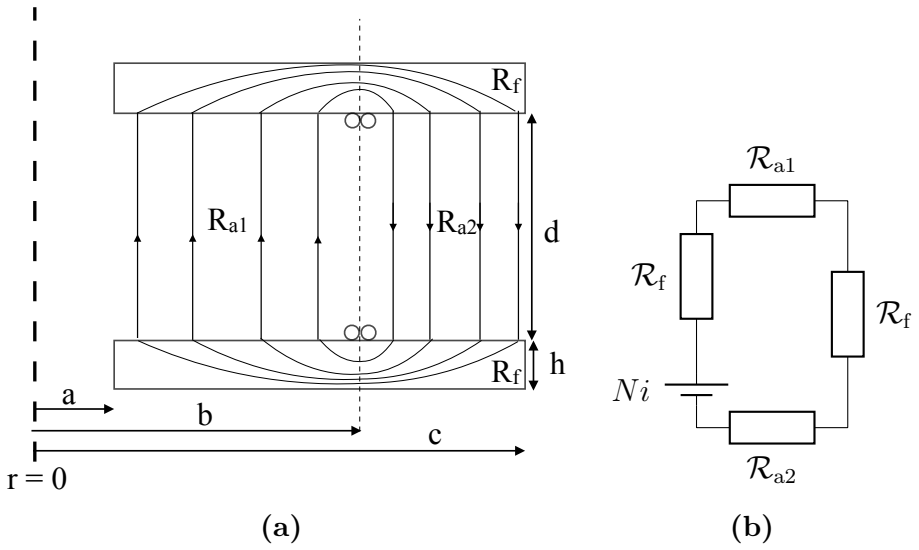

Figure 2.7: (a) Axisymmetric schematic of a energy transfer system consisting of two coils of radius b and two circular ferromagnetic plates of inner radius a, outer radius c and thickness h. The coils are separated by a distance d. (b) Circuit diagram of the magnetic circuit in Fig. 2.7(a).

there are no fringing effects of the magnetic field in the air gap and that no fields leak out from the backside of the ferrites. Then, the reluctance of the two air gaps are

$$\mathcal{R}_\mathrm{a1} = \frac{d}{\mu_0 \pi \left(b^2 - a^2\right)},$$
$$\mathcal{R}_\mathrm{a2} = \frac{d}{\mu_0 \pi \left(c^2 - b^2\right)}.$$

We approximate the magnetic flux average path in the ferromagnetic plates to extend from the radius r_1 to the radius r_2, where

$$r_1 = \frac{1}{2}(a + b),$$
$$r_2 = \frac{1}{2}(b + c).$$

Thus, we can integrate the contributions to the reluctance from ring segments of width dr, i.e.

$$d\mathcal{R} = \frac{dr}{\mu_0\mu_\mathrm{r} \cdot 2\pi r h}, \tag{2.34}$$

between r_1 and r_2 and this yields an approximate reluctance of one of the ferrites as

$$\mathcal{R}_\mathrm{f} = \frac{1}{\mu_0\mu_\mathrm{r} \cdot 2\pi h} \ln\left(\frac{r_2}{r_1}\right) = \frac{1}{\mu_0\mu_\mathrm{r} \cdot 2\pi h} \ln\left(\frac{b+c}{a+b}\right).$$

Thus, the total reluctance of the energy transfer system is

$$\mathcal{R}_\mathrm{tot} = \frac{d}{\mu_0\pi\left(b^2-a^2\right)} + \frac{d}{\mu_0\pi\left(c^2-b^2\right)} + \frac{2}{\mu_0\mu_\mathrm{r} \cdot 2\pi h} \ln\left(\frac{b+c}{a+b}\right). \tag{2.35}$$

To estimate the contributions to the total reluctance, we assume that the two air gaps have the same area. Possible parameter values that create such ferrite geometries are $a = 0.05\,\mathrm{m}$, $b = 0.26\,\mathrm{m}$ and $c = 0.37\,\mathrm{m}$. If we set the distance between the coils to $d = 0.3\,\mathrm{m}$ and the ferrite thickness to $h = 0.02\,\mathrm{m}$, the contributions to the total reluctance are

$$\begin{aligned} \mathcal{R}_\mathrm{a1} &= 1.13 \cdot 10^6\,\mathrm{H}^{-1}, \\ \mathcal{R}_\mathrm{a2} &= 1.13 \cdot 10^6\,\mathrm{H}^{-1}, \\ \mathcal{R}_\mathrm{f} &= \frac{4.45 \cdot 10^6}{\mu_\mathrm{r}}\mathrm{H}^{-1}. \end{aligned} \tag{2.36}$$

Equation (2.36) shows that if the relative permeability of the ferrites is large, e.g. $\mu_\mathrm{r} > 100$, the reluctance in the ferrites is small compared to the reluctance of the air gaps. Thus, the magnetic flux flowing through the coils is limited by the reluctance of the air gap, even if the ferrite thickness h is small.

3

Method for design and optimization

The study of the wireless energy transfer systems in this thesis is split up in three parts: (i) circuit design; (ii) coil design; and (iii) optimization. In this chapter, the circuits are studied by numerical computation. The coil design and the effects of shielding plates, ferrites and ground are studied using analytical and FEM models. The optimization varies the geometry of the coils, shielding plates and ferrites to maximize the coupling coefficient while keeping the magnetic fields within the guidelines decided by ICNIRP. The optimized coil geometry is then used together with the circuit model to optimize the power transfer and efficiency.

3.1 Circuit models

The circuit described in Chapter 2, also shown in Fig. 3.1, is analyzed using a `MATLAB` script. We solve the matrix problem in Equation (3.1)

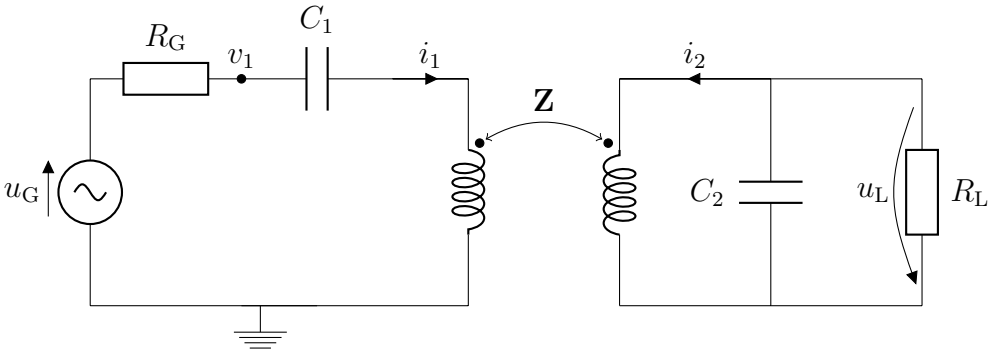

Figure 3.1: Circuit diagram with capacitor in parallel on the primary side.

$$\begin{bmatrix} \frac{1}{R_G} & 1 & 0 & 0 \\ -1 & Z_{11} + \frac{1}{j\omega C_1} & 0 & Z_{12} \\ 0 & 0 & \frac{1}{R_L} + j\omega C_2 & 1 \\ 0 & Z_{21} & -1 & Z_{22} \end{bmatrix} \begin{bmatrix} v_1 \\ i_1 \\ u_L \\ i_2 \end{bmatrix} = \begin{bmatrix} \frac{u_G}{R_G} \\ 0 \\ 0 \\ 0 \end{bmatrix}, \tag{3.1}$$

to find all currents and voltages in the circuit. Here, the impedances Z_{11}, Z_{12}, Z_{21} and Z_{22} are given in Eq. (2.26) and they are computed by FEM or by simplified analytical expressions. Given the solution to Eq. (3.1), the power dissipated in the load is given by

$$P_{\mathrm{L}} = \frac{|u_{\mathrm{L}}|^2}{R_{\mathrm{L}}},$$

and the power transfer efficiency by

$$\eta = \frac{P_{\mathrm{L}}}{\Re\left(u_{\mathrm{G}} i_1^*\right)}.$$

3.2 Coil design

The coil design study is divided into two parts. First, the effects on the coil characteristics in free space due to the geometry of the coils are analyzed. Next, we introduce conducting and magnetic materials in the geometry and study their impact. The free-space models are based on the analytical expression given in Section 2.1.2.1, while the more complicated cases in the second part are studied by means of the FEM. The coil windings are placed in a grid pattern with N_{r} (radial) and N_{z} (axial) wires. The total number of coil windings is thus $N = N_{\mathrm{r}} N_{\mathrm{z}}$.

3.2.1 Free-space coil models

The effects of the geometry of the coils are studied in free space using the expressions for the self- and mutual inductance for spatially distributed coils given in Eq. (2.15) and Eq. (2.14), respectively. In free space, the resistance of the coils only depends on the wire resistance, which is calculated by Eq. (2.17). These calculations are simple and fast and the study is done by means of parametric sweeps.

The coils are described by their geometry, material and type of wire, i.e. solid or litz wire. The geometrical parameters are the coil radius, the wire radius, the distance between wire windings, the number of windings and the location of the coils. From the expressions in Eq. (2.15) and Eq. (2.14), it is clear that both the self- and mutual inductance increase with larger coil radius and number of coil windings. Similarly, the total length of the wire, and thus the wire resistance, is directly proportional to the radius and number of windings. The wire radius influences mainly the self-inductance and resistance.

For the frequencies of interest, it is clear that the resistance of a litz wire is lower than that of a solid wire, where it is assumed that the radius of the wire strands constituting the litz wire is small enough and the total conductive area of the litz wire is comparable to the solid wire.

From Chapter 2, we know that the coupling coefficient plays an important role in the performance of a wireless energy transfer system. The coupling coefficient is

non-trivial for the spatially distributed coil system and it is this behavior that is the main focus of the parametric study for the free-space coil models.

3.2.2 Modelling of adjacent objects

The coaxial coils of the free-space models are also implemented in a FEM solver. In addition, different components present in a more realistic wireless transfer system between the ground and the bottom of a vehicle are introduced and their effects on the resistance, inductance and magnetic field is evaluated. In detail, we analyze the effect of metallic shielding plates in the ground and in the car chassis, ferrites around the coils. The FEM solver is compared to analytical expressions in Appendix B.1 and it is demonstrated that the two techniques compare well for computations of the inductance, magnetic flux, flux density, resistance and induced voltage. Further, in Appendix B.2, we investigate the convergence of the adaptive mesh refinement used in the FEM computations. After one adaptive mesh refinement, we find that the estimated error is less than 0.1% for the self-resistance, mutual resistance, self-inductance and mutual inductance.

3.2.2.1 Geometry and computational domain boundary

The magnetic fields caused by the currents in the coils tend rather slowly towards zero as the distance to the coils tend to infinity. It is impossible to solve the magnetic field problem in an infinitely large region and the computational domain is therefore extended by a so-called infinite element domain, which is terminated by the Dirichlet boundary condition $A_\varphi = 0$ on the outer boundary. Infinite elements are useful for unbounded problems, such as the one studied in this thesis, but requires that the solution varies slowly in the infinite elements [22]. This is achieved by placing the infinite element domain at a sufficiently large distance from the coils.

COMSOL's AC/DC-interface can simulate both solid and litz wire using the "single-turn" and "multi-turn" coil domains, respectively [4]. Both kinds of coil types can be excited with voltage or current sources.

An example of the geometry of the problem is shown in Fig. 3.2. The model is axisymmetric with respect to the z-axis and the computational domain is truncated by an infinite element domain. Details of the primary and secondary coils are shown in Fig. 3.3. Note that there is only metal shielding on the secondary side, which represent the vehicle chassis.

3.2.2.2 Shielding metal-plates

We study the effects of shielding the magnetic fields with metal plates both in the car and in the ground. The metal shield in the car represents the car chassis, which is usually constructed of iron. We investigate shielding from three kinds of metal:

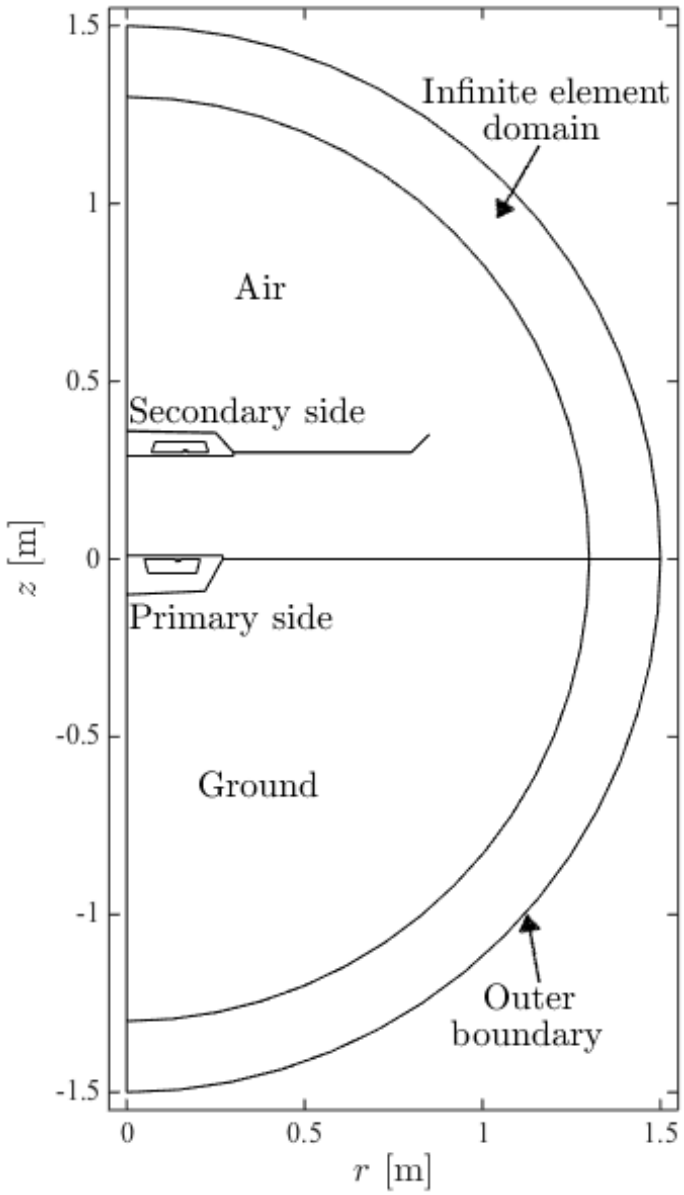

Figure 3.2: Computational geometry for a typical wireless power transfer system. The geometry is axisymmetric and the z-axis is the axis of symmetry. The primary side consists of the primary coil surrounded by ferrite. The secondary side consists of the secondary coil surrounded by ferrite. A metal plate is present to shield the region above the secondary coil from magnetic fields.

iron (highly ferromagnetic); steel (somewhat ferromagnetic); and aluminum (non-magnetic). Shielding the primary coil from ground with metal is not necessarily beneficial because it is unproblematic to have strong magnetic fields in the ground and the eddy current in metal plate typically exceed the eddy currents in the ground when the shield is absent. Therefore, we investigate two cases: (i) metal in both the car and in the ground; and (ii) metal only in the car.

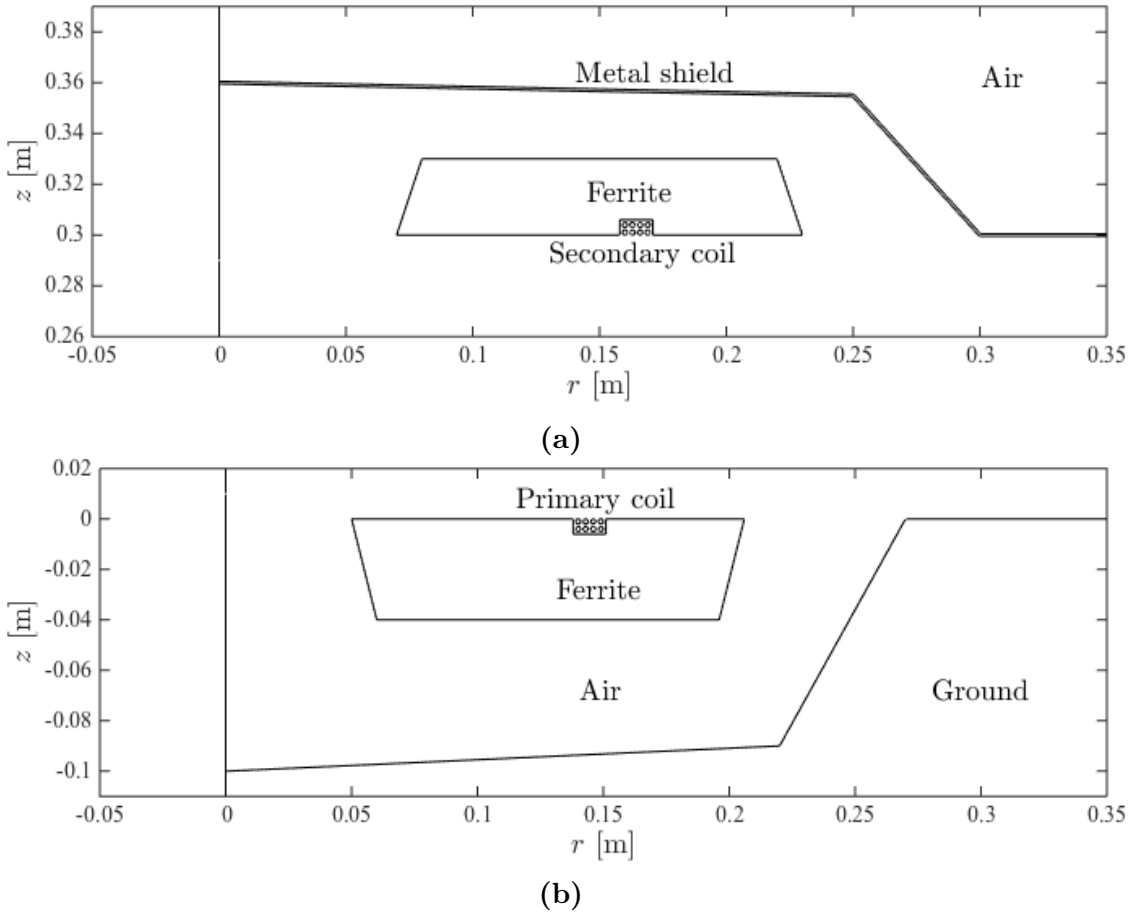

Figure 3.3: Detail of the geometry of (a) the secondary side and (b) the primary side. The geometry is axisymmetric with respect to the z-axis. The coils windings are represented as circles on a grid.

3.2.2.3 The dielectric properties of ground

The ground beneath the energy transfer system can feature both resistive and dielectric losses. The conductivity and permittivity of moist ground at radio frequencies is studied in Ref. [16], and we use these material properties to study the losses in the ground.

3.2.2.4 Estimating the magnetic flux density

To quantify the magnetic flux density magnitude, we probe the magnetic flux density at five sampling points along a vertical line at $z = 0.85\,\mathrm{m}$, which are located between the two coils. As we excite the primary coil by the current $I^{\mathrm{p}}_{\mathrm{exc}} = 1\,\mathrm{A}$, we get the magnetic flux density values $\vec{B}^{\mathrm{p}}_i$ at the five sampling points indexed $i = 1, .., 5$. Similarly, a new computation with $I^{\mathrm{s}}_{\mathrm{sec}} = 1\,\mathrm{A}$ yields B^{s}_i. We then estimate the magnetic flux density $\vec{B}_i$ at point i during operation of the wireless energy transfer

system as

$$\vec{B}_i = \vec{B}_i^{\mathrm{p}} + \vec{B}_i^{\mathrm{s}} = \left[\frac{\vec{B}_i^{\mathrm{p}}}{I_{\mathrm{exc}}^{\mathrm{p}}}\right] I_{\mathrm{circuit}}^{\mathrm{p}} + \left[\frac{\vec{B}_i^{\mathrm{s}}}{I_{\mathrm{exc}}^{\mathrm{s}}}\right] I_{\mathrm{circuit}}^{\mathrm{s}},$$

where the quantities $I_{\mathrm{circuit}}^{\mathrm{p}}$ and $I_{\mathrm{circuit}}^{\mathrm{s}}$ are the currents in the primary and secondary coil, i.e. i_1 and i_2 according to Eq. (3.1). Next, we assume that the magnitude of the currents in the two coils are equal, i.e.

$$|I_{\mathrm{circuit}}^{\mathrm{p}}| = |I_{\mathrm{circuit}}^{\mathrm{s}}| = I_{\mathrm{max}}.$$

Here, we let I_{max} be the maximum allowed current in the coils and it is limited by the specifications of the wires used for the windings in the coils. In the following, we use $I_{\mathrm{max}} = 20\,\mathrm{A}$. Further, we assume the phase difference between the currents in the two coils is 90°. With these approximations, we can estimate the worst-case magnitude of the magnetic flux density during operation as

$$\left|\vec{B}_i\right| \approx \left(\left|\left[\frac{\vec{B}_i^{\mathrm{p}}}{I_{\mathrm{exc}}^{\mathrm{p}}}\right]\right|^2 + \left|\left[\frac{\vec{B}_i^{\mathrm{s}}}{I_{\mathrm{exc}}^{\mathrm{s}}}\right]\right|^2\right)^{1/2} I_{\mathrm{max}}. \tag{3.2}$$

3.3 Coil optimization

A general, nonlinear optimization problem can be written as

$$\begin{aligned} \underset{\mathbf{x}}{\text{minimize}} \quad & f(\mathbf{x}), \\ & \mathbf{l}_{\mathrm{b}} \leq \mathbf{x} \leq \mathbf{u}_{\mathrm{b}}, \\ \text{subject to:} \quad & \mathbf{l}_{\mathrm{lin}} \leq \mathbf{A}\mathbf{x} \leq \mathbf{u}_{\mathrm{lin}}, \\ & \mathbf{l}_{\mathrm{nl}} \leq \mathbf{f}_{\mathrm{nl}}(\mathbf{x}) \leq \mathbf{u}_{\mathrm{nl}}, \end{aligned}$$

where $\mathbf{x}$ is a vector of the design parameters and $f(\mathbf{x})$ is the objective function. There are three kinds of constraints: (i) upper and lower bounds on the parameters in $\mathbf{x}$ of the form $\mathbf{l}_{\mathrm{b}} \leq \mathbf{x} \leq \mathbf{u}_{\mathrm{b}}$; (ii) linear constraints of the form $\mathbf{l}_{\mathrm{lin}} \leq \mathbf{A}\mathbf{x} \leq \mathbf{u}_{\mathrm{lin}}$; and (iii) nonlinear constraints of the form $\mathbf{l}_{\mathrm{nl}} \leq \mathbf{f}_{\mathrm{nl}}(\mathbf{x}) \leq \mathbf{u}_{\mathrm{nl}}$.

The main goal of the optimization procedure is to maximize the coupling coefficient of the two coils and, simultaneously, minimize the magnetic flux density in regions where humans (or animals) can be present.

The objective function is defined as

$$f(\mathbf{x}) = -\alpha \frac{k(\mathbf{x})}{k_{\mathrm{typ}}} + (1-\alpha) p_{\mathrm{B}}(\mathbf{x}), \tag{3.3}$$

where $\alpha \in [0, 1]$ is a weight that determines the relative importance of the two terms $-k(\mathbf{x})/k_{\mathrm{typ}}$ and $p_{\mathrm{B}}(\mathbf{x})$. Here, $k(\mathbf{x})$ is the coupling coefficient and k_{typ} is its typical

value, where we use the constant $k_{\text{typ}} = 0.1$ in the following. The penalty function $p_{\text{B}}(\mathbf{x})$ is defined as

$$p_{\text{B}}(\mathbf{x}) = \frac{\left(\frac{1}{N}\sum_{i=1}^{N=5}\left(|\vec{B}_i(\mathbf{x})|^2\right)^4\right)^{1/4}}{B_{\text{max}}^2}, \tag{3.4}$$

where $|\vec{B}_i|$ is the estimated magnetic flux density during operation of the wireless energy transfer system according to Eq. (3.2). In Eq. (3.4), the estimated magnetic flux density magnitude $\left|\vec{B}_i\right|$ is squared to make $p_{\text{B}}(\mathbf{x})$ differentiable everywhere. Further, $B_{\text{max}} = 8.84\,\mu\text{T}$ is the peak-value limit of the human exposure to magnetic fields given by ICNIRP. The parameter α is used in the following manner. We first set $\alpha = 1$ and optimize with respect to the design parameters $\mathbf{x}$. We then decrease α slightly and start a new optimization from the solution retrieved from the previous run. If the difference in α is small the optimized solution of the new objective function should be close to that of the previous. This procedure gives information on how the objective function depends on the weight α and can help us design the wireless energy transfer system with two conflicting objectives, namely $-k(\mathbf{x})/k_{\text{typ}}$ and $p_{\text{B}}(\mathbf{x})$.

3.3.1 Gradient-based optimization

The gradient descent method is a powerful first-order optimization algorithm suitable for problems where the gradient of the objective function is continuous. The method converges from the initial design in the design space towards the closest local optimum. The gradient descent method may, however, converge slowly. Unless the problem is known to be convex, it is difficult to know if an optimum is local or global.

Gradient-based optimization exploits a multivariable, continuously differentiable objective function $f(\mathbf{x})$. It starts from an initial design $\mathbf{x}_i$, where $i = 1$. Then, the gradient of $f(\mathbf{x})$ at $\mathbf{x} = \mathbf{x}_i$ is evaluated and corresponds to the direction in which $f(\mathbf{x})$ increases fastest. Given a position $\mathbf{x}_i$ in solution space, we find the next position at

$$\mathbf{x}_{i+1} = \mathbf{x}_i - \gamma\nabla f(\mathbf{x}_i),$$

where the step size γ is either set to an appropriate value or calculated using a line search.

For gradient-based optimization to be reliable, the errors in the gradient computations must be sufficiently small. The error in the FEM computations is less than 0.1% after one adaptive mesh refinement, as described in Section 3.2.2. In the following FEM computations, we use one adaptive mesh refinement to ensure that the error in the gradient computations are sufficiently low.

The gradient of the objective function in (3.3) is

$$\nabla f(\mathbf{x}) = -\frac{\alpha}{k_{\text{typ}}}\nabla k(\mathbf{x}) + (1-\alpha)\nabla p_{\text{B}}(\mathbf{x}).$$

In this thesis, we use central finite-differences to estimate the gradient, e.g. the derivative of function $g(\mathbf{x})$ with respect to parameter x_j is estimated by

$$\frac{\partial g}{\partial x_j} \approx \frac{g\left(\mathbf{x} + \mathbf{e}_j \frac{\Delta x_j}{2}\right) - g\left(\mathbf{x} - \mathbf{e}_j \frac{\Delta x_j}{2}\right)}{\Delta x_j}, \tag{3.5}$$

where $\mathbf{e}_j$ is a unit vector with zero entries except for element k that is set to zero. The gradient of $p_{\mathrm{B}}(\mathbf{x})$ is calculated using Eq. (3.5) directly. The gradient of the coupling coefficient is found using the product rule

$$\frac{\partial k}{\partial x_j} = \left\{ k = \frac{M}{\sqrt{L_1 L_2}} \right\} = \frac{\partial k}{\partial M}\frac{\partial M}{\partial x_j} + \frac{\partial k}{\partial L_1}\frac{\partial L_1}{\partial x_j} + \frac{\partial k}{\partial L_2}\frac{\partial L_2}{\partial x_j},$$

where

$$\begin{aligned}
\frac{\partial k}{\partial M} &= \frac{1}{\sqrt{L_1 L_2}}, \\
\frac{\partial k}{\partial L_1} &= -\frac{1}{2}\frac{L_2 M}{(L_1 L_2)^{3/2}}, \\
\frac{\partial k}{\partial L_2} &= -\frac{1}{2}\frac{L_1 M}{(L_1 L_2)^{3/2}}.
\end{aligned}$$

The derivative of the coupling coefficient may then be written as

$$\frac{\partial k}{\partial x_j} = k\left(\frac{1}{M}\frac{\partial M}{\partial x_j} - \frac{1}{2L_1}\frac{\partial L_1}{\partial x_j} - \frac{1}{2L_2}\frac{\partial L_2}{\partial x_j}\right).$$

The derivatives of M, L_1 and L_2 with respect to x_j are given by Eq. (3.5).

3.3.2 Geometrical constraints

The coil geometry is restricted is several ways. The length of the coil wire is limited by the estimated maximum length so that each individual coil (primary or secondary) does not become self-resonant, as discussed in Section 2.1.2.3. This restricts the number of turns for the coil and their individual radii. The ferrite geometries are restricted such that the thickness of the ferrite is sufficiently large for manufacturing purposes. In Fig. 3.4, a possible ferrite geometry on the primary side is shown with a name label for each corner. The positions of the corners Ac, Bc, Cc and Dc are derived from the geometry of the coil, e.g. outer coil radius, number of windings, wire radius, etc., and are not explicitly optimized. The r- and z-coordinates of the corners Af, Bf, Cf and Df are free to move as long as the following constraints are satisfied

$$\begin{aligned}
r_{\mathrm{Ac}} - r_{\mathrm{Af}} &\geq 15\,\mathrm{mm}, \\
z_{\mathrm{Af}} &= z_{\mathrm{Ac}}, \\
r_{\mathrm{Bc}} - r_{\mathrm{Bf}} &\geq 15\,\mathrm{mm}, \\
r_{\mathrm{Cf}} - r_{\mathrm{Cc}} &\geq 15\,\mathrm{mm}, \\
r_{\mathrm{Df}} - r_{\mathrm{Dc}} &\geq 15\,\mathrm{mm}, \\
z_{\mathrm{Df}} &= z_{\mathrm{Dc}}.
\end{aligned} \tag{3.6}$$

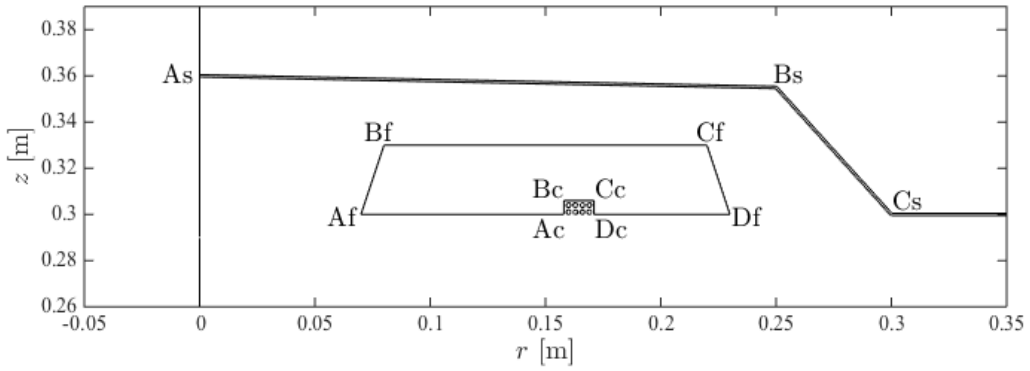

(a)

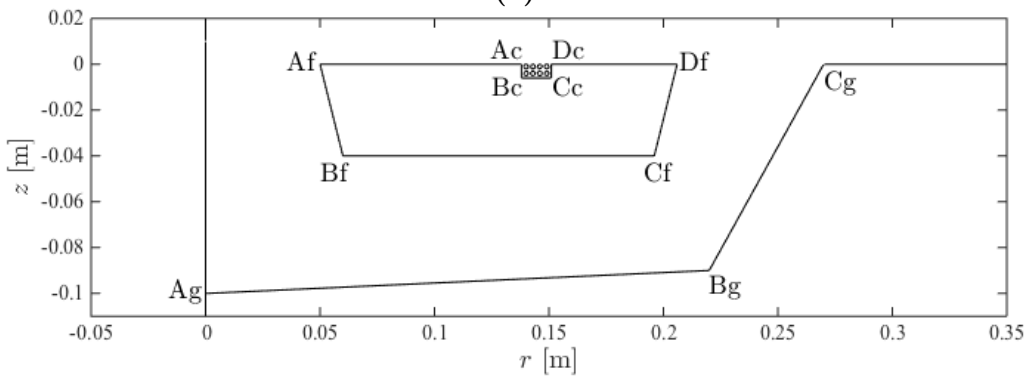

(b)

Figure 3.4: Schematic of a possible geometry of (a) the secondary side and (b) the primary side, with name labels for each corner.

The constraints in Eq. (3.6) apply to both the primary and secondary side. Further, we restrict the primary and secondary side individually as

$$
\begin{aligned}
&\text{Primary side:} && \text{Secondary side:}\\
&z_{\mathrm{Bc}} - z_{\mathrm{Bf}} \geq 15\,\mathrm{mm} && z_{\mathrm{Bf}} - z_{\mathrm{Bc}} \geq 15\,\mathrm{mm},\\
&z_{\mathrm{Cc}} - z_{\mathrm{Cf}} \geq 15\,\mathrm{mm}, && z_{\mathrm{Cf}} - z_{\mathrm{Cc}} \geq 15\,\mathrm{mm},\\
&z_{\mathrm{Bf}} - z_{\mathrm{Ag}} \geq 15\,\mathrm{mm}, && z_{\mathrm{Cf}} - z_{\mathrm{Cc}} \geq 15\,\mathrm{mm},\\
&z_{\mathrm{Cf}} - z_{\mathrm{Ag}} \geq 15\,\mathrm{mm}, && z_{\mathrm{As}} - z_{\mathrm{Bf}} \geq 15\,\mathrm{mm},\\
&z_{\mathrm{Bf}} - z_{\mathrm{Bg}} \geq 15\,\mathrm{mm}, && z_{\mathrm{As}} - z_{\mathrm{Cf}} \geq 15\,\mathrm{mm},\\
&z_{\mathrm{Cf}} - z_{\mathrm{Bg}} \geq 15\,\mathrm{mm}, && z_{\mathrm{Bs}} - z_{\mathrm{Bf}} \geq 15\,\mathrm{mm},\\
&r_{\mathrm{Bg}} - r_{\mathrm{Cf}} \geq 15\,\mathrm{mm}, && r_{\mathrm{Bs}} - r_{\mathrm{Cf}} \geq 15\,\mathrm{mm},\\
&r_{\mathrm{Cg}} - r_{\mathrm{Df}} \geq 15\,\mathrm{mm}, && r_{\mathrm{Cs}} - r_{\mathrm{Df}} \geq 15\,\mathrm{mm},\\
&z_{\mathrm{Cg}} = z_{\mathrm{Df}}, && z_{\mathrm{Cs}} = z_{\mathrm{Df}}.
\end{aligned}
\tag{3.7}
$$

3.4 Circuit optimization

The impedance matrix of a an optimized wireless energy transfer coil geometry is inserted into the circuit in Fig. 3.1 and the circuit components are optimized. The two most important performance parameters of the circuit is its efficiency η and the power P_{L} dissipated in the load resistance. The objective function is therefore defined as

$$f(\mathbf{x}) = \beta \frac{1}{\eta(\mathbf{x})} + (1-\beta)\frac{P_{\mathrm{typ}}}{P_{\mathrm{L}}(\mathbf{x})}, \tag{3.8}$$

where $P_{\mathrm{typ}} = 1000\,\mathrm{W}$ is a typical (constant) value of the transferred power. The components subject to optimization is C_1, C_2, R_{L} and u_{G} and the objective function is evaluated at 85 kHz. The weight β, similar to α in Eq. (3.3), determines the relative importance of the efficiency as compared to the power dissipated in the load. The generator resistance is kept constant at $400\,\mathrm{m\Omega}$, in accordance with Section 2.1.2.5.

The gradient of the objective function in Eq. (3.8) is a complicated function of the values of all circuit components. However, the circuit equation in Eq. (3.1) relatively cheap to compute and the gradient can be found using finite-differences.

3.4.1 Circuit component constraints and initialization

The generator voltage is limited to the range of 0 V to 250 V and the load resistance is limited values between $0\,\Omega$ and $500\,\Omega$. The two capacitors C_1 and C_2 are not explicitly limited. Instead, the resonance frequencies of the two resonating circuits that compose the wireless energy transfer system are limited to the range 65 kHz to 105 kHz. As the resonance frequency depends on both the capacitance and inductance of the resonator, see Eq. (2.3), the upper and lower limits for the capacitors depend on the self-inductance of the chosen coil design.

Ten separate optimizations are carried out for every value of β in the objective function in Eq. (3.8). Each optimization is initialized with randomly assigned circuit optimization parameters and the optimized circuit design with the lowest objective function is then selected as the best candidate for the particular value chosen for β. This procedure increases the chance of avoiding local minima and it is feasible for this optimization problem since the circuit problem is computationally cheap.

4

Results

This chapter presents the results produced by the parametric studies, the effects of different materials in proximity to the coils, and finally the optimization results.

4.1 Coil design

In this section, we present the results of computations based on coil models in free space and with adjacent objects, such as ground and metal shields. First, we present how the coupling coefficient depends on the coil geometry in free space. Next, we investigate the effects of adjacent objects on the coupling coefficient, resistance and magnetic field.

4.1.1 Free-space coil models

We compute k between two identical coils with fixed wire radius and coil distance h in free space. First, the outer coil radius r_0 is varied, while all other geometry parameters are kept constant. The results are presented in Fig. 4.1. We find, from Fig. 4.1, that the coupling coefficient is approximately proportional to the ratio r_0/h around $r_0/h = 1$. In the context of a wireless power transfer system, it is desirable to maximize the coupling coefficient and, consequently, it is useful to make the radii of the two coils as large as possible in relation to their distance of separation for the free-space situation.

Next, we fix the outer radius of the coils to 0.3 m and vary the number of coil windings. The distance between two coil windings is 10 mm. The results from the sweep of N_r and N_z are presented in Fig. 4.2. The coupling coefficient shows a non-trivial behavior when N_r and N_z are varied. Noticeably, the maximum coupling coefficient is not found for the highest number of coil windings, and it is concluded that flat coils $N_\mathrm{z} = 1$ with about $N_\mathrm{r} = 15$ turns yield the largest coupling coefficient, where the air gap between the coils is $h = 0.3\,\mathrm{m}$.

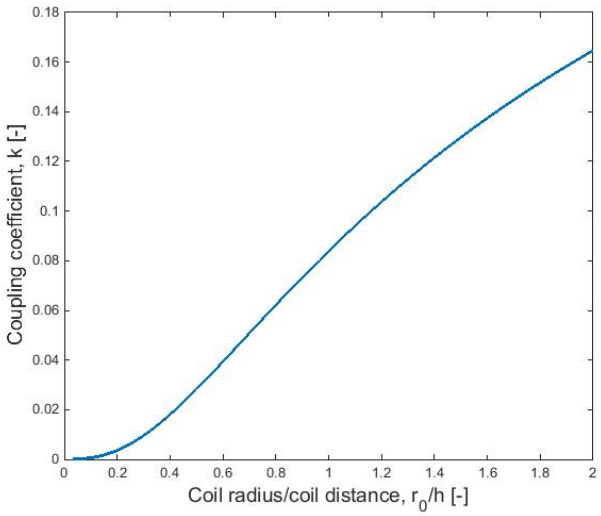

Figure 4.1: Coupling coefficient as a function of coil radius r_0 divided by the coil distance h. The two coils are kept identical throughout the parameter sweep.

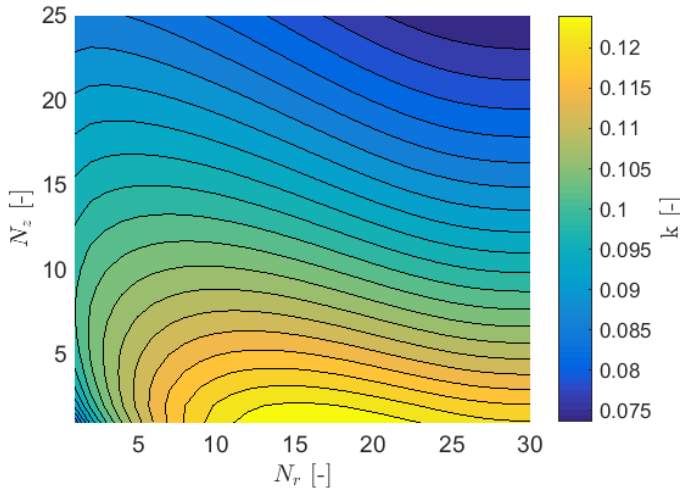

Figure 4.2: Coupling coefficient between two identical coils as a function of number of coil windings in radial and axial direction. Wire radius, distance between coil loops and the coil distance are fixed during the parameter sweep.

4.1.2 Coil models with adjacent objects

In the following sections, we study the effects on the inductance, losses and magnetic fields due to shielding plates, ferrites and ground. The two coils are identical and fixed with an outer radius equal to 0.3 m. Here, we use a wire radius of 3 mm for a litz wire with a strand density of 0.9. The coils are wound with $N_\mathrm{r} = 4$ times $N_\mathrm{z} = 2$ turns in a grid, where the distance between the wires is 7 mm. The vertical distance between the coils is 0.3 m. As a reference case, we use these coils located in free space. The FEM model in free space yields the inductances, resistances and

magnetic fields given in Tab. 4.1. The magnetic field lines and magnitude for a current excitation of 1 A through both coils is shown in Fig. 4.3.

Table 4.1: Inductances, resistances and coupling coefficient for two coils in free space.

	Free space
R_1, R_2	10.8 mΩ
R_{12}	0
L_1, L_2	81.5 μH
M	7.93 μH
k	0.0973

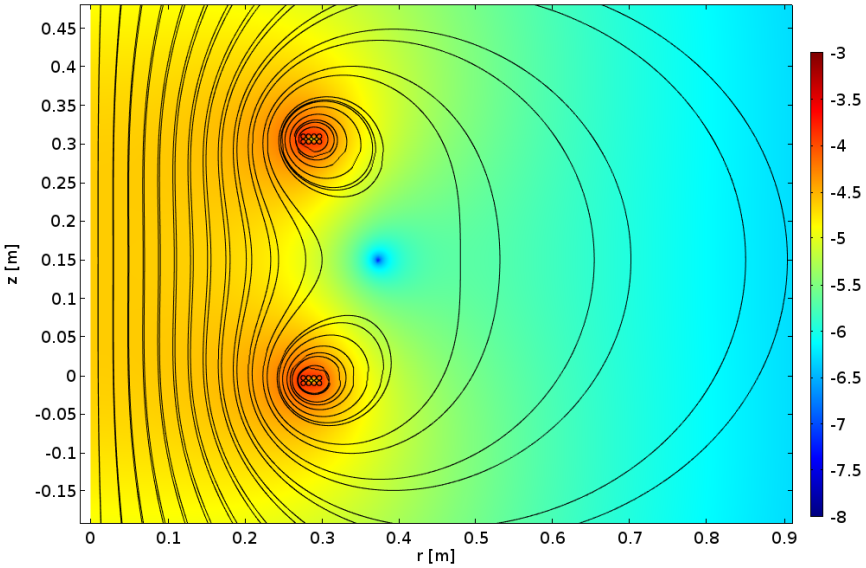

Figure 4.3: Magnetic field lines and $\log_{10}|\vec{B}|$ for two coils in free space and an excitation current of 1 A in both coils.

4.1.2.1 Metal shielding

Metallic plates are placed in the vicinity of the two coils to confine the magnetic field between the coils, as shown in Fig. 4.4(a). Iron is the most common car chassis material but we also investigate shields made of steel and aluminum. These materials are chosen as they are common, cheap and have different permeabilities. Aluminum is essentially non-magnetic whereas stainless steel ($\mu_r = 100$) and pure iron ($\mu_r = 4000$) are ferromagnetic. Given the results in Section 2.2.1, we expect the resistive losses to increase and the coupling coefficient to decrease as the eddy currents in the metals dissipate energy and reduces the magnetic flux through the coils. Table 4.2 presents the effects of adding metal plates in both the ground and in the car. The table shows that by adding the metal plates, we have increased

Table 4.2: Inductances, resistances and coupling coefficient with metal shields of iron, steel and aluminum in both the car and ground and only in the car.

	Shield in both car and ground			Shield only in car
	Iron	Steel	Aluminum	Aluminum
μ_r	4000	100	1	1
R_1	1.09 Ω	0.55 Ω	27.2 mΩ	11.9 mΩ
R_2	2.44 Ω	1.15 Ω	38.7 mΩ	38.7 mΩ
R_{12}	0.267 Ω	0.114 Ω	2.98 mΩ	3.13 mΩ
L_1	68.0 μH	66.4 μH	65.2 μH	79.6 μH
L_2	59.2 μH	55.8 μH	53.5 μH	53.6 μH
M	1.99 μH	1.66 μH	1.44 μH	2.42 μH
k	0.0314	0.0273	0.0243	0.0371

the resistive losses and decreased the inductances and coupling coefficient when compared to the situation with the same coils located in free space, which we use as a reference case. The difference in the coupling coefficient is small as we compare the three metals. However, the aluminum plate affects the resistance significantly less than the ferromagnetic metals. Figure 4.4(a) shows the magnetic field strength and field lines when the aluminum plates are included. It is clearly visible from Fig. 4.4(a) that the aluminum efficiently confines the magnetic fields between the coils. The current density in the top plate is shown in Fig. 4.4(b) and the induced surface current density is clearly visible. We conclude that adding metal shielding severely decreases the coupling coefficient and increases the resistances. Aluminum reduces the coupling coefficient slightly more than steel and iron, but the resistive losses in the aluminum is significantly lower than the losses in the ferromagnetic metals. If we leave out the metal shielding in the ground and only shield the car chassis, the reduction in the coupling coefficient and the increase in resistance is less severe, which is shown in the last column in Tab. 4.2.

4.1.2.2 Ferrite plates

To guide the magnetic fields and reduce the reluctance of the magnetic circuit, we add a ferrite plate below the primary coil and another ferrite plate above the secondary coil. The ferrite material has a relative permeability of $\mu_r = 3000$ and a conductivity of $\sigma = 10^{-12}\,\mathrm{S/m}$. The ferrite is similar to the ferrite "F Material" from Magnetics inc. [11]. However, the ferrite used in this thesis has constant permeability and conductivity while these material properties depends on the frequency, magnetic flux density and temperature for the "F Material". The expression in Eq. (2.18) limits the length of the wire used for the coil and the maximum length of the wire is

$$l_{\max} = \frac{c_0}{2f_0\sqrt{\xi\mu_r^{\mathrm{eff}}}} = \frac{c_0}{2f_0\sqrt{\xi\left(\mu_r+1\right)/2}} \approx 14.4\,\mathrm{m}, \tag{4.1}$$

for the relative permeability $\mu_r = 3000$, $f_0 = 85\,\mathrm{kHz}$ and $\xi = 10$. It is reasonable to limit the outer radius of the coils to 0.3 m in order to make it fit a normal car. A

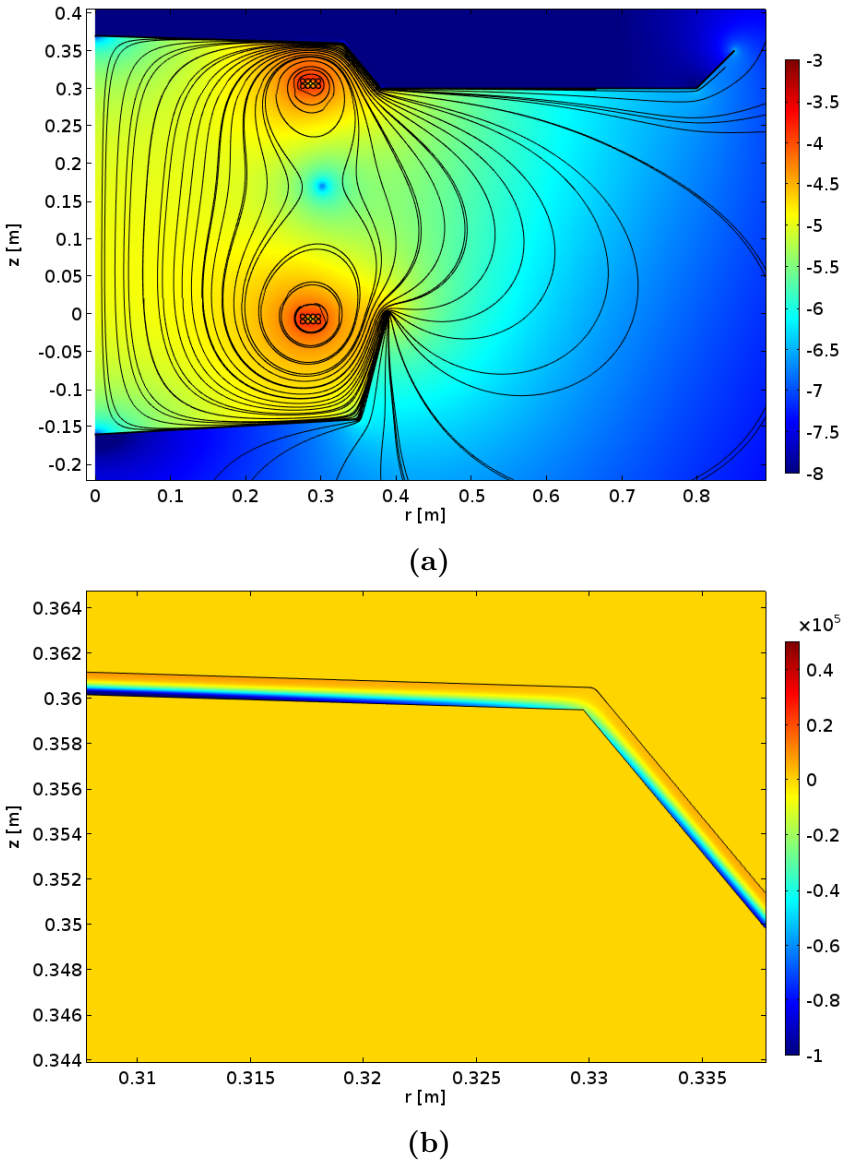

Figure 4.4: (a) Magnetic field lines and $\log_{10}|\vec{B}|$ and (b) induced current density $\vec{J}$ in the aluminum shield above the secondary coil. Both coils are excited with a current of 1 A.

coil with $N_r = 4$ and $N_z = 2$ and an outer radius 0.3 m has a total wire length of 14.4 m and may be a suitable choice in the energy transfer system.

Figure Fig. 4.5 shows two cases in order to study how the performance varies with the addition of highly magnetic and nonconductive materials: (a) small amount of ferrite material; and (b) large and thick ferrite plates. The material parameters and the geometry of the ferrites are identical for the primary and secondary coil. Thus, the self-resistance and self-inductance is equal for the two coils and these results are shown in Tab. 4.3. The ferrite adds an insignificant amount of resistive losses to the system. The large ferrite plates increases the coupling by almost 50% as compared to the free-space case, while the small core geometry decreases the coupling. The

Table 4.3: Inductances, resistances and coupling coefficient with ferrite material added in the vicinity of the primary and secondary coil.

	Small ferrite	Large ferrite
R_1, R_2	10.8 mΩ	10.8 mΩ
R_{12}	6.7 nΩ	120 nΩ
L_1, L_2	161 μH	193 μH
M	1.23 μH	26.5 μH
k	0.0765	0.137

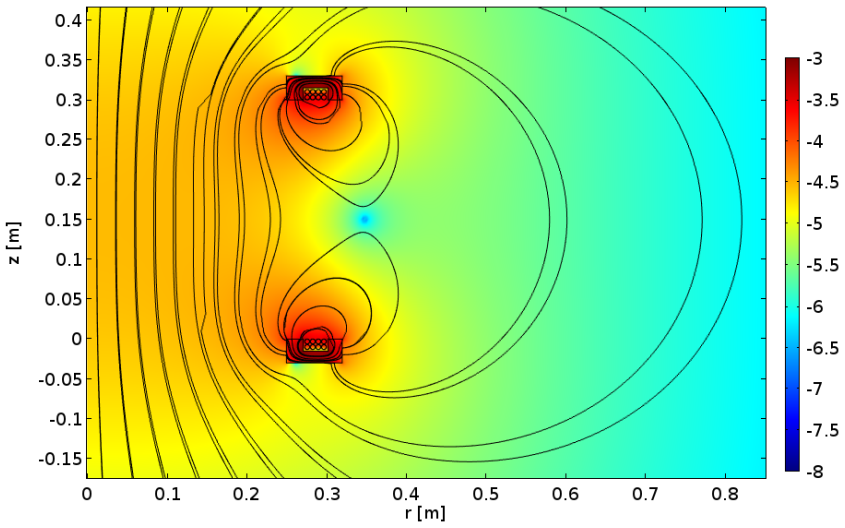

(a)

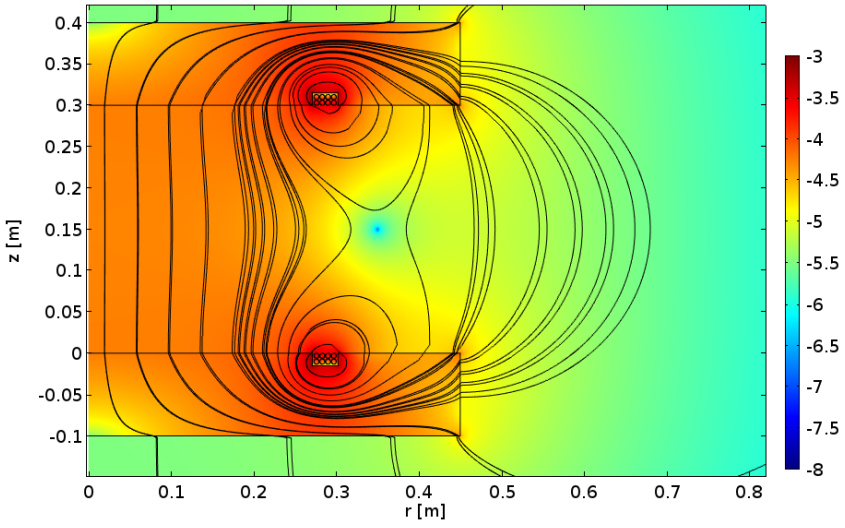

(b)

Figure 4.5: Magnetic field lines and $\log_{10}|\vec{B}|$ for (a) relatively small ferrites of annular shape and (b) large and thick ferrite plates. Both coils are excited with a current of 1 A.

magnetic field for the two cases are plotted in Fig. 4.5. The magnetic field strength is significantly increased in the region between the coils for the large ferrite plates. We can clearly see that the magnetic fields are guided by the large ferrite plates and that the field strength on the "backside" of the ferrite plate is several orders of magnitude lower than between the coils. Thus, the large ferrite plates efficiently guides the magnetic fields and they provide some shielding, which can be used to reduce the induced currents in e.g. the metal in the car chassis.

4.1.2.3 Ground

The study in Ref. [16] shows that the conductivity in the ground can reach several mS/m at 100 kHz, when the water content of the soil varies from dry to 40 weight-%. For the same interval of moisture content, the relative permeability varies from 2 to around 100. Even though the conductivity of the soil is rather low, the ground can still contribute to resistive and dielectric losses. At 100 kHz and a water content of 15 weight-%, the ground conductivity is 5.6 mS/m and the relative permittivity is 50, which gives a loss tangent of

$$\tan\delta = \frac{\sigma}{\omega\varepsilon} \approx 20.$$

This indicates that the displacement current in the ground is negligible as compared to the conduction current.

Ground with a water content of 15% is introduced as shown in Fig. 4.6. The conduc-

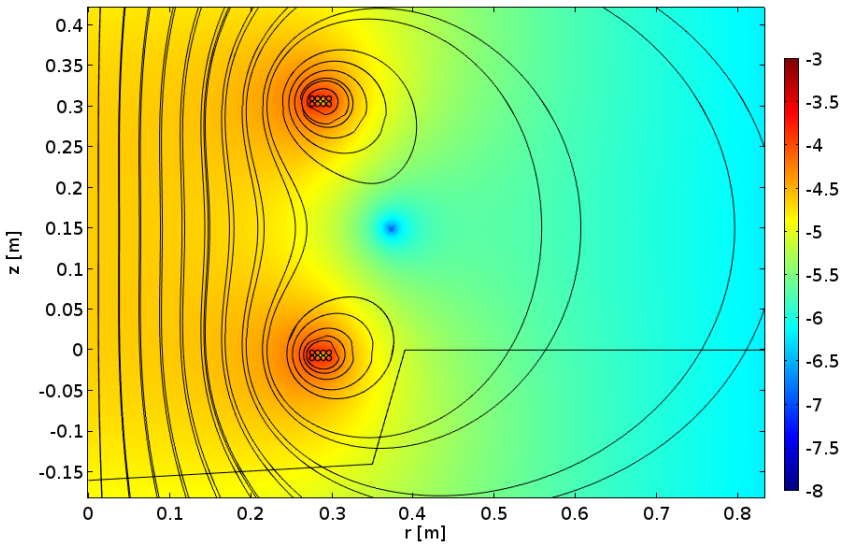

Figure 4.6: Magnetic field lines and $\log_{10}|\vec{B}|$ for two coils with ground as shown in Fig. 3.2. Both coils are excited with a current of 1 A.

tivity and permittivity is interpolated from Ref. [16], while the relative permeability is assumed to unity. The results are shown in Tab. 4.4 and we notice that the resistances are slightly increased by the proximity of lossy ground, but no other effect is clearly visible.

Table 4.4: Inductances, resistances and coupling coefficient with ferrite core surrounding the coils.

	Ground
R_1	11.8 mΩ
R_2	11.2 mΩ
R_{12}	0.537 mΩ
L_1	81.5 μH
L_2	81.5 μH
M	79.3 μH
k	0.0973

4.1.3 Optimized coil geometry

From Section 4.1.2, it is clear that placing metal shields in-between the primary coil and the ground is detrimental to the performance of the energy transfer system. In addition, such shielding is rarely needed in order to protect humans or electrical equipment from the magnetic field and it implies additional costs for the wireless power transfer system. We also know that ferrite plates is useful for guiding the magnetic flux and the magnetic field in the air is. Section 2.2.2 shows us that the reluctance is dominated by the air gap between the coils and, thus, the ferrites can be made thin and they do not necessarily need to have very large relative permeabilities. Next, we use the objective function in Eq. (3.3) and run the optimization with the constraints in Eq. (3.6) and Eq. (3.7), where $\mu_\mathrm{r} = 100$ for the ferrite material. In Fig. 4.7, the coupling coefficient is plotted against the magnetic field penalty function for varying α. Note that the first optimization is started with $\alpha = 1$ and consecutive optimizations with lower α are initialized with the optimized design based on the previous value of α. The optimized geometries of the four points in Fig. 4.7 indicated by $\alpha = 1$, 0.98, 0.94 and 0.9 are shown in Fig. 4.8. In Fig. 4.8(a), the initial ferrite design is outlined with dashed lines. Figure 4.8(a) shows us that maximum coupling coefficient is achieved with the largest ferrite surface area. This is in agreement with the investigations of the reluctance in Sec. 2.2.2. When α is reduced, the width of the ferrites is decreased and the magnetic field in the nearby region where humans may be present is reduced. It is interesting to note that the ferrite plate on the primary side is affected less than the ferrite plate on the secondary side by the reduction of α. Thus, the shape of the ferrite on the secondary side is more important in order to reduce the magnetic field than the primary side ferrite. Note that the horizontal part of the metal shield plate on the secondary side follows the ferrites closely. This behavior is unexpected, because nearby metal plates are expected to reduce the coupling coefficient. However, the metal plate also reduce the magnetic field strength in the region where humans may be present. The electric and magnetic properties of the geometries in Fig. 4.8 are presented in Tab. 4.5.

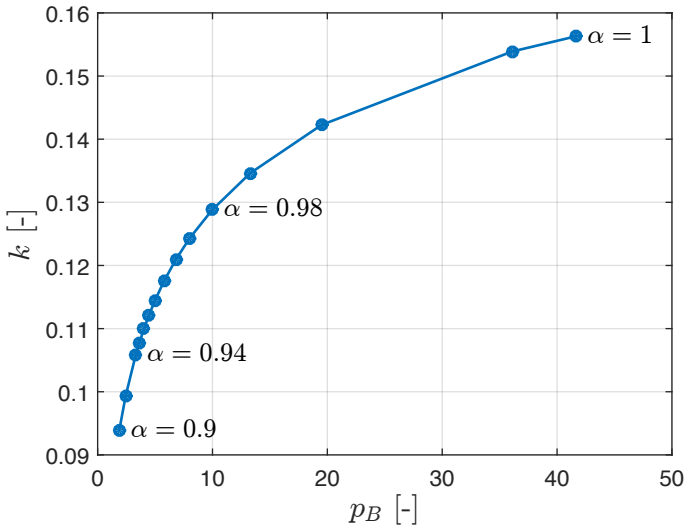

Figure 4.7: Coupling coefficient as a function of the magnetic field penalty function P_B for $\alpha \in [0.9, 1]$.

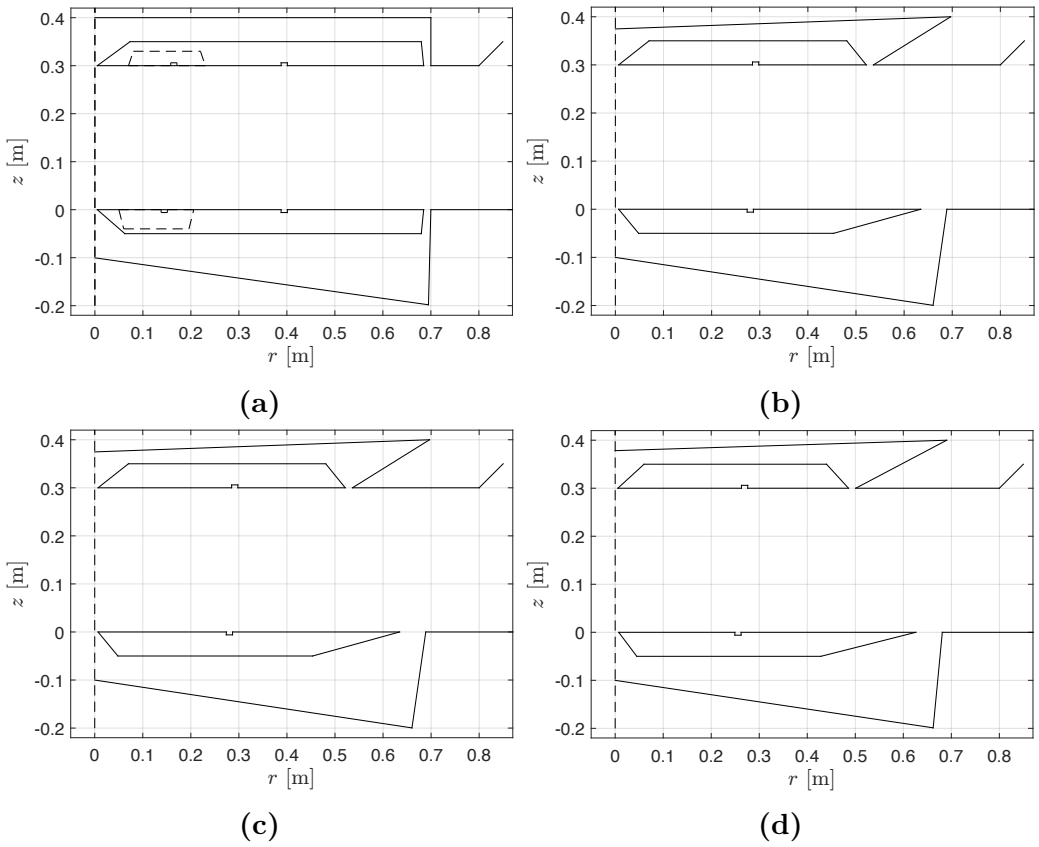

Figure 4.8: Geometries optimized with (a) $\alpha = 1$, (b) $\alpha = 0.98$, (c) $\alpha = 0.94$ and (d) $\alpha = 0.9$. In Fig. 4.8(a) the initial ferrite design is shown with dashed lines. The remaining optimized geometries was initialized from the optimized design of a previous optimization with a slightly higher α.

Table 4.5: Inductance, resistance, coupling coefficient and p_B for the geometries shown in Fig. 4.8.

α	1	0.98	0.94	0.9
R_1 [mΩ]	127	105	89.1	80.9
R_2 [mΩ]	129	109	95.3	88.1
R_{12} [mΩ]	6.77	5.23	4.28	3.69
L_1 [μH]	331	266	219	196
L_2 [μH]	330	271	228	207
M [μH]	51.7	34.5	23.7	18.9
k [-]	0.156	0.129	0.106	0.0939
p_B [-]	41.6	9.98	3.32	1.88

4.2 Optimized wireless energy transfer system

The impedance matrices of the four designs shown in Fig. 4.8 are exploited in the context of the circuit optimization with the objective function given in Eq. (3.8). We optimize the circuits for different values of β in Eq. (3.8) and plot the efficiency as a function of power dissipated in the load in Fig. 4.9. Figure 4.9 shows that we

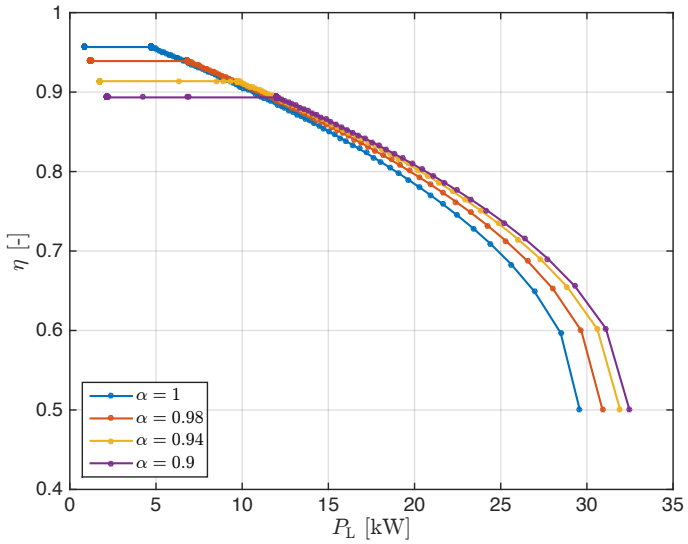

Figure 4.9: Efficiency and power dissipated in the load for circuits optimized with α varying from zero to one for the four geometries shown in Fig. 4.8.

can achieve efficiencies around 90% with all geometries. Similarly, the maximum achievable amount of transferred power is 30 kW, but the efficiency is then reduced to 50%. Note that the highest transferred power is achieved with the design with the lowest coupling coefficient.

In Fig. 4.10, the current in the primary coil is plotted as a function of the transferred power and we find that high power requires large currents. We also find that the current-power characteristic only differs between the different designs at low and

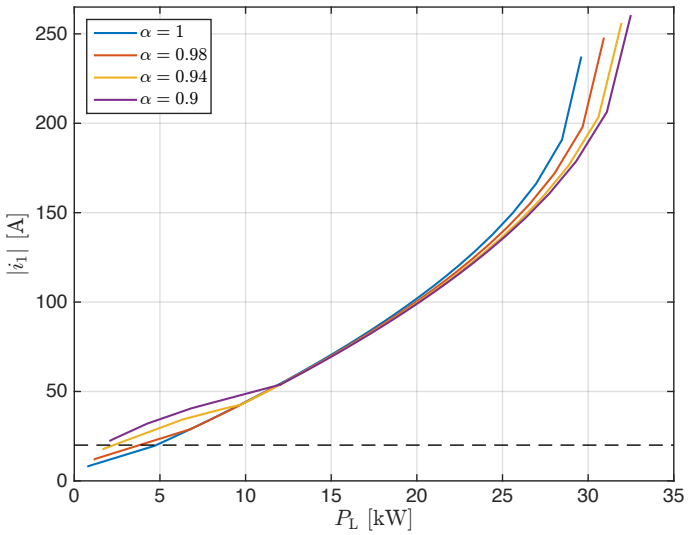

Figure 4.10: Current in the primary coil as a function of transferred in the load for circuits optimized with β varying from zero to one for the four geometries shown in Fig. 4.8.

high levels of transmitted power. In the intermediate zone, the optimized circuits behave similarly. To prevent overheating of the energy transfer system, we limit the magnitude of the currents. As described in Sec. 3.2.2.4, we restrict the the largest current in the two coils to 20 A and use the circuit design with the highest efficiency and transferred power given this current constraint to find the performance of the system. The resulting circuits and coil currents are presented in Tab. 4.6. Disregarding the magnitudes of the magnetic fields, it is clear that the design with

Table 4.6: Optimized performance, component values and coil currents for the four geometries in Fig. 4.8. The optimized circuit with the highest efficiency and transferred power with the current closest to 20 A is chosen and rescaled such that the largest current is at the limit.

α	1	0.98	0.94	0.9
k	0.156	0.129	0.106	0.0939
$\max_{i=1,\ldots,5} \lvert\vec{B}\rvert$ [μT]	47.15	22.16	13.37	10.15
η	0.96	0.94	0.91	0.89
P_L [kW]	4.80	3.24	2.15	1.66
R_L [Ω]	500	500	500	500
u_G [V]	250	173	117	93
C_1 [nF]	10.8	13.4	16.2	18.0
C_2 [nF]	10.2	12.9	15.4	16.9
f_1 [kHz]	84.3	84.3	84.5	84.6
f_2 [kHz]	86.9	85.1	85.5	85.0
i_1 [A]	$20.0\angle 0.00°$	$20.0\angle 0.35°$	$20.0\angle 0.11°$	$20.0\angle -0.15°$
i_2 [A]	$8.98\angle -103.2°$	$9.16\angle -105.3°$	$8.76\angle -103.3°$	$8.44\angle -102.4°$

the highest coupling coefficient achieves the highest amount of transferred power. The efficiency varies little in all designs presented in Tab. 4.6. Notably, the magnitude of the current in the secondary coil is less than half the magnitude of the current in the primary coil. Table 4.6 shows an increase in the coupling coefficient, power delivered to the load and the transfer efficiency as we increase α. This is similar to the expressions for the power and efficiency derived in Appendix A. Thus, if we allow larger magnetic fields, i.e. α close to unity, we can achieve higher coupling coefficient, transferred power and efficiency.

The magnetic flux density magnitude for the four geometries in Fig. 4.8 with the currents given in Tab. 4.6 are shown in Fig. 4.11. The decrease in magnetic field

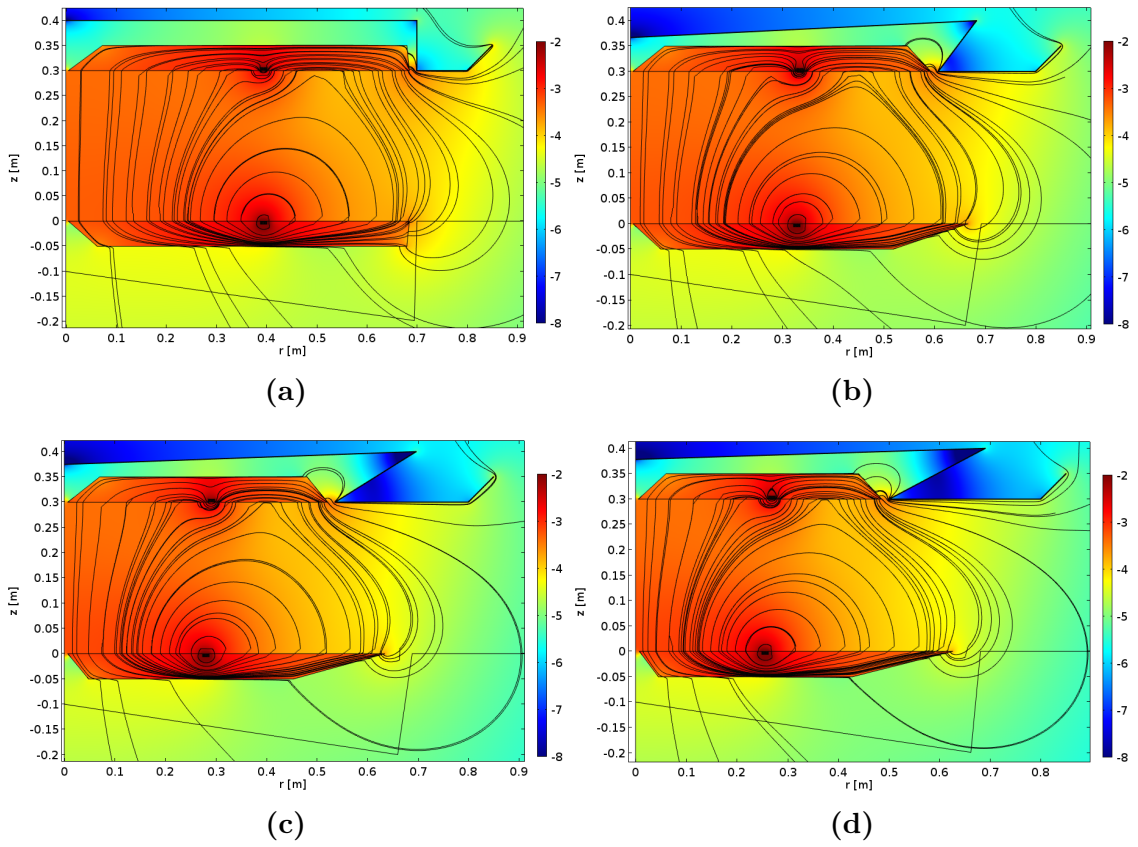

Figure 4.11: Magnetic field lines and $\log_{10}|\vec{B}|$ of the four geometries in Fig. 4.8 optimized with (a) $\alpha = 1$, (b) $\alpha = 0.98$, (c) $\alpha = 0.94$ and (d) $\alpha = 0.9$. The currents through the coils are given in Tab. 4.6.

strength toward the edge of the car is clearly visible as the four magnetic field plots in Fig. 4.11 are compared. The maximum magnetic flux density probed at the five points along the vertical line at $r = 0.85\,\mathrm{m}$ for the studied geometries, are presented in the second row of Tab. 4.6. All magnetic flux density values in Tab. 4.6 exceed the $8.84\,\mu\mathrm{T}$ limit given by ICNIRP. However, as the magnetic fields scale linearly with the currents through the coils, we can reduce the magnetic fields by decreasing the applied voltage u_G. The amount of transferred power is given in Tab. 4.7 as the the applied voltage u_G is reduced such that the magnetic flux density at the

edge of the car does not exceed 8.84 μT, where we have used the circuit designs given in Tab. 4.6. Table 4.7 shows that the amount of power delivered to the load is considerably reduced compared to the transferred power in Tab. 4.6. Thus, we

Table 4.7: Power transferred with the optimized circuits in Tab. 4.6 with applied voltage reduced such that the magnetic field where humans or animals can be present does not exceed the peak-value limit of 8.84 μT given by ICNIRP.

α	1	0.98	0.94	0.9
u_{G} [V]	47	69	77	81
P_{L} [kW]	0.17	0.52	0.94	1.3

could gain a significant amount of transferred power, should we be able to allow for larger magnetic fields or an increase of the distance from the coils to places humans or animals can be located. This is made clear in Fig. 4.12, where the magnitude of the magnetic flux density is plotted along a horizontal line at $z = 0.15\,\mathrm{m}$, i.e. in the middle between the two coils, for the design in Fig. 4.8(d). The rapid decay of the magnetic flux density is clearly visible from approximately $r = 0.4\,\mathrm{m}$.

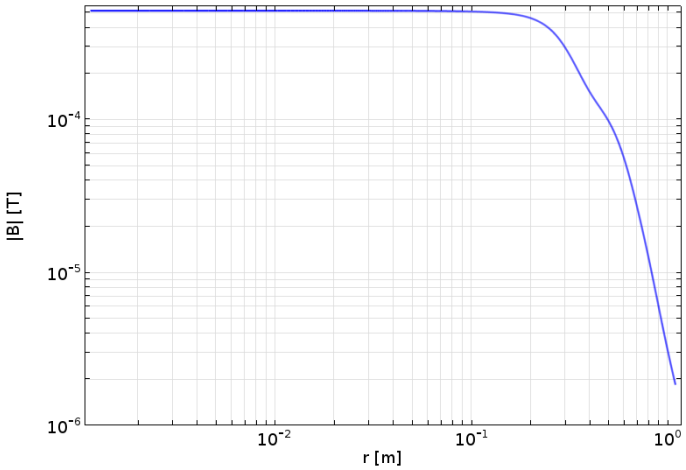

Figure 4.12: Magnetic field strength in logarithmic scale along a horizontal line at $z = 0.15\,\mathrm{m}$ during operation of the wireless energy transfer system with design as in Fig. 4.8(d), with optimized circuit components and currents in the coils given in Tab. 4.6.

5

Conclusions and future work

In this thesis, we study wireless energy transfer systems based on resonant inductive coupling with application to the charging of electric vehicles. The work also investigates the implications of metal plates, ferrites and ground adjacent to the energy transfer system. In this chapter, the main outcome of the thesis is presented together with what should be focused on in future studies.

5.1 Conclusions

We investigate and design a wireless energy transfer system based on two inductively coupled resonant circuits separated by an air gap. We show that the coupled wireless energy transfer system has two resonance peaks and that the separation of these peaks increase with increasing coupling coefficient. The coils are studied in the frequency domain with axisymmetric geometry. To avoid the self-resonance of the coils, we limit the length of the coil wire such that the self-resonance frequency appears at much higher frequencies than the frequency of operation. We study the potential higher frequency components generated by the power source and show that basically only the fundamental frequency is present in wireless energy transfer systems based on resonant inductive coupling. Further, we discuss the effects of adding materials in the vicinity of the coils. We show that metal plates above the secondary coil can efficiently shield the surrounding from magnetic fields. However, the magnetic fields induce eddy currents in the metal plates, which drastically decrease the coupling coefficient and increases the resistive losses. Ferrites, a material with very low eddy currents and high permeability, is placed on both the primary and secondary side and it is shown to efficiently cancel the negative effects of the shielding plates and improve the coupling coefficient. The geometry of the coils, metal plates and the ferrites is optimized using gradient-based optimization in order to maximize the coupling coefficient and keep the magnetic field low in regions where humans may be present. The wireless energy transfer system circuit components are also optimized using gradient-based optimization methods using the impedance matrices that result from the optimization of the geometry based on field computations.

Given a parameter study of two identical and co-axial coils in free space, we find that the coupling coefficient increases monotonically with r/d, where r is their common radius and d is the distance between the coils. Adding conductive and ferromagnetic

materials in the vicinity of the coil have varying effects on the coupling coefficient and losses of the energy transfer system. Metal plates can drastically lower the coupling coefficient and increase the resistive losses. However, the metal plates can efficiently shield the interior of the car from magnetic fields and protect the passengers from the potentially harmful magnetic fields. To limit the undesirable effects of the metallic shield, we use ferrites to guide the magnetic fields in such a manner that induced currents in the metal shields are low. Well-designed ferrites can completely cancel the negative effects of the metal shields. From studying the reluctance of a simplified model of the system, we find that the relative permeability of the ferrites does not need to be very large and $\mu_{\mathrm{r}} \approx 100$ can be sufficient for some situations.

For the optimized coil geometries, we achieve coupling coefficients between 0.09 and 0.15. The width of the ferrite plates has a strong influence on the coupling coefficient. The coupling coefficient increases as the width of the ferrite plates increases. When we penalize the magnetic field strength, the widths of the ferrite plates decrease since it makes the magnetic fields become more localized to the symmetry axis of the transformer and, therefore, weaker in regions where humans may be present. This width reduction is more prominent on the secondary side than the primary side. The shape of the metal chassis under the car can also be used to affect the magnitude of the magnetic fields by shielding the surroundings to some extent.

Given the optimized coil geometries and their corresponding impedance matrices, we optimize the performance of the wireless energy transfer system circuit by tuning the remaining circuit components. Without constraints on the currents in the coils, we can transfer several tens of kW. Limiting the current to 20 A in the coils, we can achieve transferred power levels of a few kW. However, even with limited currents, the magnitude of the magnetic field exceed the limits given by ICNIRP. Restricting the currents in the coils further, we can transfer approximately 1.3 kW with 89% efficiency without exceeding the 8.84 μT peak-value limitation. This is achieved with the optimized coil geometry, where we used a large penalization on the magnetic field strength and this resulted in a coupling coefficient of 0.09.

5.2 Future work

In this thesis, the magnetic field computations are performed on axisymmetrical and two-dimensional model geometries. This simplifies the computations but decreases the applicability of the model. Non-axisymmetric models in three dimensions are necessary to model real-world applications.

One such three-dimensional aspect is the potential misalignment of the two coils. A study of the effects of misalignment would yield information on how sensitive the system performance is to the displacements of the coils e.g. due to incorrect parking of the vehicle. If it is shown that the energy transfer is exceedingly sensitive, it may be necessary to equip the system with the ability to move the coils. The simulations are also carried out in the frequency domain and they do not account for

non-linearities that occur in a realistic implementations of a wireless power transfer system for , e.g., charging applications. One such non-linear effect occurs in ferromagnetic materials as they are magnetized. In the context of charging by means of a wireless power transfer system, more important non-linear effects are associated with circuit components such as diodes and transistors, which are used in rectifiers and power inverters. Other non-linearities that may be of importance are associated with power dissipation in components of the system, where the electrical behavior of the component depends on its temperature. However, temperature drift occurs on rather slow time-scales in comparison with non-linearities associated with the switching of transistors and diodes, which prompts for different treatment of the two types of non-linearities.

The simulations are also carried out in the frequency domain, which does not model the nonlinearity of the ferromagnetic materials. Further simulations in the time-domain is needed to understand the nonlinearities.

The limits for the magnetic field strength used in this thesis are based on the guidelines given by ICNIRP. These guidelines are for whole-body exposure of magnetic fields. As the fields are mainly confined to the region below the car, the human exposure is limited to the feet and lower legs. This can potentially allow us to increase the current passing through the coils and thereby increase the transferred power. This would require investigations of the magnitudes of the induced currents in the exposed parts of the human body.

Co-optimization of the coil geometry and the wireless energy transfer circuit is a potential continuation of the work in this thesis. We simplified the optimization by separating the optimization of the geometry and the circuits. This separation is feasible because the coupling coefficient depends only on the geometrical properties of the coils and the efficiency and power delivered to the load increases with the coupling coefficient. However, a large coupling coefficient is not the only factor in a well-performing wireless energy transfer system. Co-optimization of the geometry and circuit components allows for synergy effects and potentially better performing designs.

Bibliography

[1] Min Chen and Gabriel a. Rincón-Mora. Accurate electrical battery model capable of predicting runtime and I-V performance. *IEEE Transactions on Energy Conversion*, 21(2):504–511, 2006.

[2] D. K. Cheng. *Fundamentals of Engineering Electromagnetics*. Addison-Wesley, 1993.

[3] COMSOL Multiphysics. http://www.comsol.com/.

[4] COMSOL Multiphysics. *AD/DC Module User's Guide*. 2013.

[5] John Conway and Nield J. A. Sloan. *Sphere Packings, Lattices and Groups*, volume 290. Springer, third edit edition, January 1999.

[6] R. S. Duncan and H. A. Stone. A Survey of the Application of Ferrites to Inductor Design. *Proceedings of the IRE*, pages 2–3, 1955.

[7] ICNIRP. ICNIRP Guidelines for limiting exposure to time varying electric, magnetic and electromagnetic fields (up to 300 GHz). *Health Physics*, 74(4):494–523, 1998.

[8] J. D. Jackson. *Classical Electrodynamics*. Wiley, New York, 3rd. edition, 1999.

[9] Mehdi Kiani and Maysam Ghovanloo. The circuit theory behind coupled-mode magnetic resonance-based wireless power transmission. *IEEE Transactions on Circuits and Systems I: Regular Papers*, 59:2065–2074, 2012.

[10] André Kurs, Aristeidis Karalis, Robert Moffatt, J D Joannopoulos, Peter Fisher, and Marin Soljacic. Wireless power transfer via strongly coupled magnetic resonances. *Science (New York, N.Y.)*, 317(2007):83–86, 2007.

[11] Magnetics. F Materials (http://www.mag-inc.com/products/ferrite-cores/f-material), 2015.

[12] Antonio Massarini and Marian K. Kazimierczuk. Self-capacitance of inductors. *IEEE Transactions on Power Electronics*, 12(4):671–676, 1997.

[13] F. Mazaleyrat and L. K. Varga. Ferromagnetic nanocomposites. *Journal of Magnetism and Magnetic Materials*, 215:253–259, 2000.

[14] C.D. Owens. A Survey of the Properties and Applications of Ferrites below Microwave Frequencies. *Proceedings of the IRE*, 44:1234–1248, 1956.

[15] Thomas Rylander, Pär Ingelström, and Anders Bondeson. *Computational Electromagnetics*. Springer, second edition, 2013.

[16] R. L. Smith-Rose. The Electrical Properties of Soil for Alternating Currents at Radio Frequencies, 1933.

[17] Charles R. Sullivan. Optimal choice for number of strands in a litz-wire transformer winding. *IEEE Transactions on Power Electronics*, 14(2):283–291, 1999.

[18] N. Tesla. World System of Wireless Transmission of Energy. *Telegraph and Telegraph Age*, pages 1–4, 1927.

[19] The MathWorks - MATLAB version 2014b. *http://www.mathworks.se*. The MathWorks Inc., Natick, Massachusetts, 2015.

[20] TOMLAB. http://tomopt.com/.

[21] Stanimir Valtchev, Elena Baikova, and Luis Jorge. Electromagnetic field as the wireless transporter of energy. *Facta universitatis - series: Electronics and Energetics*, 25(3):171–181, 2012.

[22] O C Zienkiewicz, C Emson, and P Bettess. Novel Boundary Infinite Element. *International Journal for Numerical Methods in Engineering*, 19(3):393–404, 1983.

A

Circuit model analysis

It is possible to analytically solve the system of equations that describes the wireless energy transfer circuit. However, the results are non-trivial to interpret. In this section, we simplify the problem in order to derive expressions of the efficiency and power delivered to the load that are informative and simple to understand.

A.1 Power delivered to the load

This chapter contains analytical derivations of the power dissipated in the load on the secondary side due to a current through the primary coil. We assume small coupling coefficients and that the primary side induce voltage in the secondary coil, but we neglect the voltage induced in the primary coil due to the current in the secondary coil. The circuit diagram used in the derivations is shown in Fig. A.1.

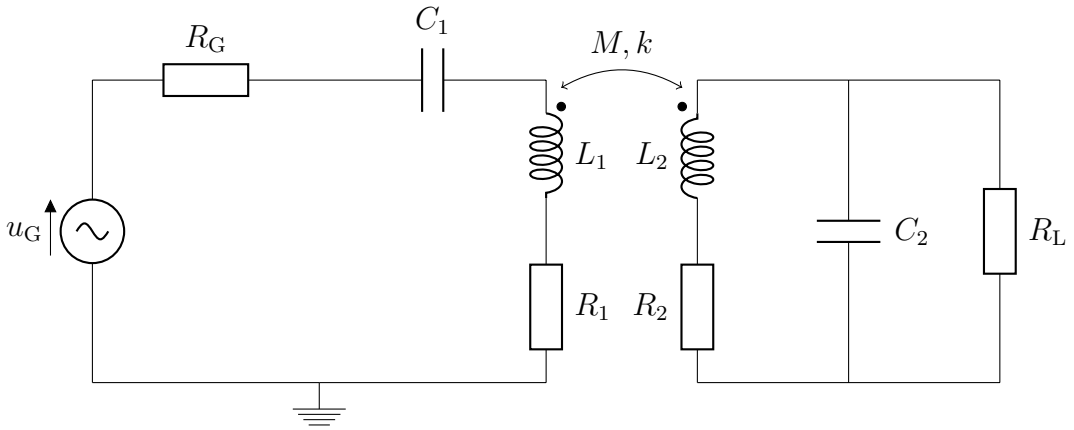

Figure A.1: Circuit diagram with capacitor in series on the primary side.

A circuit diagram of the series capacitor primary side circuit is shown in Fig. A.2. The current through inductance L_1 is found by

$$i_1 = \frac{u_G}{Z_{tot}} = \frac{u_G}{R_G + R_1 + j\omega L_1 + \frac{1}{j\omega C_1}}$$

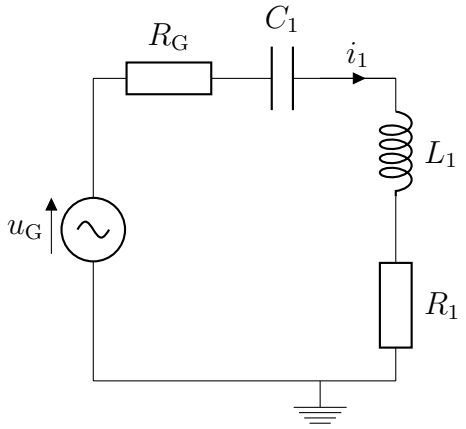

Figure A.2: Circuit diagram of the primary side with capacitor in series.

where the induced voltage in the primary coil due to i_2 is neglected. At resonance the reactive parts of the impedance cancel and the circuit can be described by the resistances R_G and R_1 connected in series with the voltage source. The current through L_1 is then

$$i_1 = \frac{u_G}{R_1 + R_G}. \tag{A.1}$$

The secondary side comprises the secondary coil L_2, a capacitor C_2 and the load resistor R_L. The circuit is excited by voltage induced by the primary coil. A circuit diagram is shown in Fig. A.3. With a current i_1 in the primary coil, the voltage

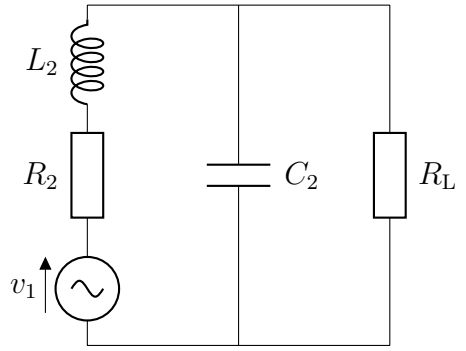

Figure A.3: Circuit diagram of the secondary side.

induced over the secondary coil is

$$v_1 = j\omega M i_1,$$

where ω is the frequency of the voltage source u_G and M is the mutual inductance between L_1 and L_2.

The impedance of the secondary side can be expressed as

$$Z = R_2 + j\omega L_2 + \frac{1}{\frac{1}{R_L} + j\omega C_2},$$

which can be rewritten as

$$Z = R_2 + \frac{R_\mathrm{L}}{1+(\omega C_2 R_\mathrm{L})^2} + j\omega L_2 + \frac{1}{j\omega C_2}\frac{(\omega C_2 R_\mathrm{L})^2}{1+(\omega C_2 R_\mathrm{L})^2}. \tag{A.2}$$

We see that we can rewrite Eq. (A.2) as a resistor, an inductor and a capacitor connected in series, with the equivalent component values

$$\begin{cases} R_\mathrm{E} = R_2 + \frac{R_\mathrm{L}}{1+(\omega C_2 R_\mathrm{L})} \\ L_\mathrm{E} = L_2 \\ C_\mathrm{E} = C_2 \frac{1+(\omega C_2 R_\mathrm{L})^2}{(\omega C_2 R_\mathrm{L})^2} \end{cases} \tag{A.3}$$

The diagram of the equivalent circuit is shown in Fig. A.4.

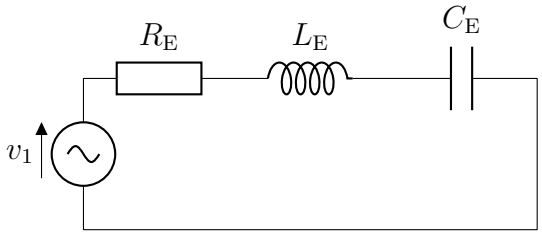

Figure A.4: Series circuit equivalent to Fig. A.3 with component values given in Eq. (A.3)

The quality factor of an electromagnetic resonator is defined as

$$Q = \omega \frac{W_\mathrm{M} + W_\mathrm{E}}{P_\mathrm{loss}},$$

where W_M and W_E are the total magnetic and electric energies respectively. At resonance the electric and magnetic energies are equal, $W_\mathrm{M} = W_\mathrm{E}$, which gives a quality factor

$$Q = \omega_0 \frac{2W_\mathrm{M}}{P_\mathrm{loss}}.$$

The magnetic energy for the resonator is defined as

$$W_\mathrm{M} = \frac{1}{2} L i^2,$$

and the resistive losses

$$P_\mathrm{loss} = R_\mathrm{E} i^2.$$

This gives us the quality factor of the equivalent circuit as

$$Q_\mathrm{E} = \omega_0 \frac{2\frac{1}{2} L_\mathrm{E} i^2}{i^2 R_\mathrm{E}} = \omega_0 \frac{L_\mathrm{E}}{R_\mathrm{E}} = \left\{ \omega_0 = \frac{1}{\sqrt{L_\mathrm{E} C_\mathrm{E}}} \quad \text{at resonance} \right\} = \frac{1}{\omega_0 C_\mathrm{E} R_\mathrm{E}}.$$

If we assume the resistance of the secondary coil to be zero, i.e.

$$R_2 = 0, \tag{A.4}$$

the quality factor becomes

$$Q_{\mathrm{E}} = \frac{1}{\omega_0 C_2 \frac{1+(\omega_0 C_2 R_{\mathrm{L}})^2}{(\omega_0 C_2 R_{\mathrm{L}})^2} \frac{R_{\mathrm{L}}}{1+(\omega_0 C_2 R_{\mathrm{L}})^2}} = \omega_0 C_2 R_{\mathrm{L}},$$

and

$$R_{\mathrm{E}} = \frac{R_{\mathrm{L}}}{1+Q_{\mathrm{E}}^2}$$
$$C_{\mathrm{E}} = C_2 \frac{1+Q_{\mathrm{E}}^2}{Q_{\mathrm{E}}^2}$$

We can now express the impedance in Eq. (A.2) in terms of the equivalent circuit quality factor as

$$Z = \frac{R_{\mathrm{L}}}{1+Q_{\mathrm{E}}^2} + j\omega_0 L_2 + \frac{Q_{\mathrm{E}}^2}{j\omega_0 C_2 \left(1+Q_{\mathrm{E}}\right)^2}$$

Next, we assume the equivalent circuit quality factor to be large, i.e.

$$Q_{\mathrm{E}} = \omega_0 R_{\mathrm{L}} C_2 \gg 1. \tag{A.5}$$

Then, the expressions for the equivalent resistance, capacitance and impedance becomes

$$\begin{aligned} R_{\mathrm{E}} &\approx \frac{R_{\mathrm{L}}}{Q_{\mathrm{E}}^2} \\ C_{\mathrm{E}} &\approx C_2 \\ Z &\approx \frac{R_{\mathrm{L}}}{Q_{\mathrm{E}}^2} + j\omega_0 L_2 + \frac{1}{j\omega_0 C_2} = \left\{\omega_0 = \frac{1}{\sqrt{L_2 C_2}}\right\} = \frac{\omega_0 L_2}{Q_{\mathrm{E}}} \end{aligned} \tag{A.6}$$

We see from Eq. (A.6) that the impedance of the secondary side can be reduced by increasing the quality factor of the equivalent circuit in Fig. A.4. With $u = v_1 = j\omega_0 M i_1$ the complex power in the secondary side becomes

$$S = \frac{|j\omega_0 M i_1|^2}{\frac{\omega_0 L_2}{Q_{\mathrm{E}}}} = \frac{\omega_0 M^2 Q_{\mathrm{E}} |i_1|^2}{L_2} = k^2 \frac{L_1}{L_2} R_{\mathrm{L}} |i_1|^2. \tag{A.7}$$

Note that the complex power is real-valued at resonance. If the secondary side is not resonating, the quality factor Q_{E} can not be defined in the same way as we have done here. We can see from Eq. (A.7) that we can influence the dissipated power on the secondary side by controlling the quality factor and the current in the primary side.

A.2 Transfer efficiency

One of the figures of merit of the energy transfer system is the efficiency. This is studied in Kiani et al. in Ref. [9]. The following derivation of the transmission efficiency is a reproduction of their results.

The circuit diagram of the wireless energy transfer system used in this thesis is showed in Fig. A.5. Note that there is no explicit generator resistance. We assume that the resistance R_1 includes both the coil resistance and the generator resistance. First, the system is assumed to be at resonance. The quality factors of the two

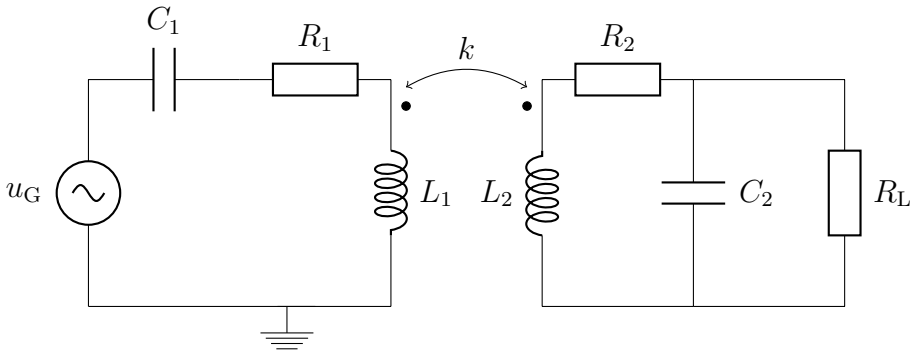

Figure A.5: Circuit diagram of two-coil transfer system.

resonant circuits are then defined as

$$Q_1 = \frac{\omega_0 L_1}{R_1} = \frac{1}{\omega_0 C_1 R_1}$$
$$Q_2 = \frac{\omega_0 L_2}{R_2} = \frac{1}{\omega_0 C_2 R_2}$$

The mutual induction between L_1 and L_2 is $M = k\sqrt{L_1 L_2}$. The derivation is now split up into three parts: (i) constructing an equivalent parallel circuit to the secondary side; (ii) constructing an equivalent circuit containing only L_2, (iii) and lastly finding an analytic expression for the total efficiency of the system.

A.2.1 Equivalent parallel circuit

We can describe the secondary side circuit with the equivalent parallel circuit shown in Fig. A.6. We can find the values of L_{p2} and R_{p2} by matching the admittance of

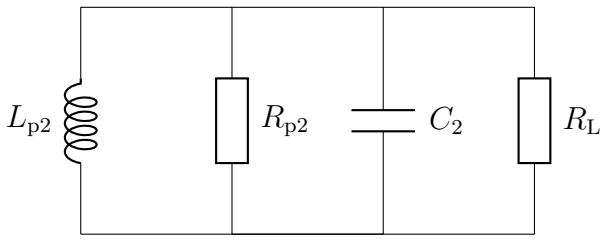

Figure A.6: Equivalent circuit diagram to the secondary side in Fig. A.5.

these two components, i.e.

$$Y_1 = \frac{1}{R_{\mathrm{p2}}} + \frac{1}{j\omega_0 L_{\mathrm{p2}}},$$

with the admittance of the inductor and resistor in the original circuit,

$$Y_2 = \frac{1}{R_2 + j\omega_0 L_2} = \frac{R_2 - j\omega_0 L_2}{R_2^2 + (\omega L_2)^2} = \frac{1}{R_2}\frac{1}{1 + \left(\frac{\omega L_2}{R_2}\right)^2} + \frac{1}{j\omega_0 L_2}\frac{1}{\left(\frac{R_2}{\omega L_2}\right)^2 + 1}$$

with $Q_2 = \omega L_2 / R_2$, we can write Y_2 as

$$Y_2 = \frac{1}{R_2}\frac{1}{1 + Q_2^2} + \frac{1}{j\omega_0 L_2}\frac{1}{1 + Q_2^{-2}}$$

For large Q_2, i.e. $Q_2 \gg 1$, the admittance simplifies to

$$Y_2 = \frac{1}{Q_2^2 R_2} + \frac{1}{j\omega_0 L_2}$$

and the equivalent circuit components becomes

$$R_{\mathrm{p}2} = Q_2^2 R_2$$
$$L_{\mathrm{p}2} = L_2$$

Next, we combine the equivalent circuit resistance with the load resistance and define the parallel resistance R_{p} as

$$R_{\mathrm{p}} = \frac{R_{\mathrm{p}2} R_{\mathrm{L}}}{R_{\mathrm{p}2} + R_{\mathrm{L}}} = \frac{Q_2^2 R_2 R_{\mathrm{L}}}{Q_2^2 R_2 + R_{\mathrm{L}}}. \tag{A.8}$$

Thus, with the assumptions that the secondary side is resonating and that the quality factor Q_2 is large, we can construct the simplified version of the secondary side shown in Fig. A.6, with R_{p} given in Eq. (A.8).

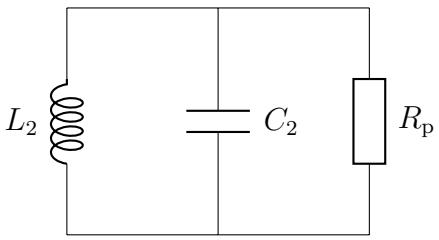

Figure A.7: Simplified circuit diagram of Fig. A.6.

A.2.2 Combining the primary and secondary sides

A non-ideal transformer can, without approximations, be rewritten as a single circuit by reflecting the secondary side onto the primary. The two circuits are shown in Fig. A.8, where the potentials u_1 and u_2 are defined as

$$u_1 = j\omega_0 L_1 i_1 + j\omega_0 M i_2,$$
$$u_2 = j\omega_0 L_2 i_2 + j\omega_0 M i_1.$$

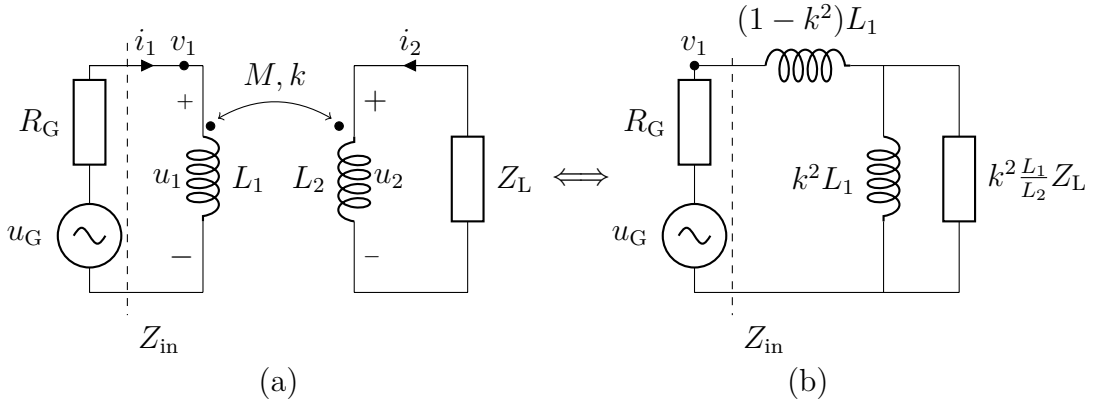

Figure A.8: (a) A non-ideal transformer and (b) its equivalent circuit.

With Kirchhoff's voltage law

$$u_2 + i_2 Z_L = 0,$$

we can find the current in the secondary side as

$$i_2 = -\frac{j\omega_0 M}{j\omega_0 L_2 + Z_L} i_1.$$

This allows us express the voltage over the primary coil in terms of i_1 and the circuit components,

$$u_1 = j\omega_0 L_1 i_1 + j\omega_0 M \left(-\frac{j\omega_0 M}{j\omega_0 L_2 + Z_L} i_1 \right) = \left(j\omega_0 L_1 + \frac{(\omega M)^2}{j\omega_0 L_2 + Z_L} \right) i_1.$$

We define the fraction u_1/i_1 as the input impedance Z_{in}. With $M^2 = k^2 L_1 L_2$ we can express the input impedance as

$$Z_{in} = \frac{(k^2-1)\omega^2 L_1 L_2 + j\omega_0 L_1 Z_L}{j\omega_0 L_2 + Z_L}.$$

The equivalence between the two circuits is proven by expressing the input impedance of the equivalent circuit in Fig. A.8(b) as

$$Z_{in,eq} = j\omega_0(1-k^2)L_1 + \frac{1}{\frac{1}{j\omega_0 k^2 L_1} + \frac{1}{k^2 \frac{L_1}{L_2} Z_L}} = \frac{(k^2-1)\omega^2 L_1 L_2 + j\omega_0 L_1 Z_L}{Z_L + j\omega_0 L_2}.$$

A.2.3 Efficiency

With the results in Section A.2.1 and A.2.2, we can construct a circuit equivalent to the circuit in Fig. A.5. This equivalent circuit is shown in Fig. A.9. The values of the reflected components C_{ref} and R_{ref} are found from the equality

$$\frac{1}{\frac{1}{R_{ref}} + j\omega_0 C_{ref}} = k^2 \frac{L_1}{L_2} Z_L = k^2 \frac{L_1}{L_2} \frac{1}{\frac{1}{R_p} + j\omega_0 C_2}.$$

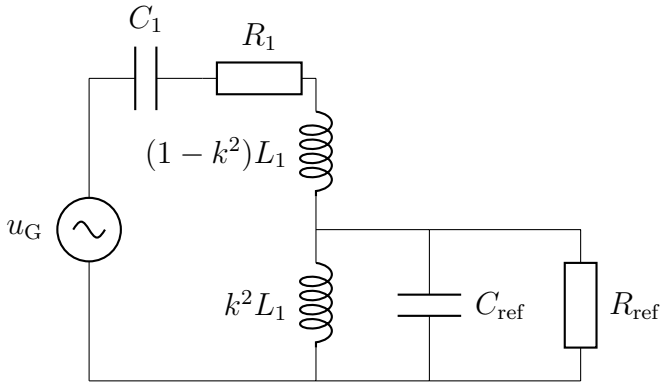

Figure A.9: Equivalent circuit seen from the voltage source.

We match the real and imaginary parts to find

$$R_\mathrm{ref} = k^2 \frac{L_1}{L_2} R_\mathrm{p},$$
$$C_\mathrm{ref} = \frac{C_2}{k^2 \frac{L_1}{L_2}},$$

where R_p is defined in Eq. (A.8).

We define the loaded quality factor of the reflected secondary side as

$$Q_\mathrm{2L} = \frac{R_\mathrm{p}}{\omega_0 L_2}, \tag{A.9}$$

and use that $C_2 = 1/(\omega_0^2 L_2)$ at resonance, to express the reflected components R_ref and C_ref as

$$\begin{aligned} R_\mathrm{ref} &= k^2 \omega_0 L_1 Q_\mathrm{2L}, \\ C_\mathrm{ref} &= \frac{L_2 C_2}{k^2 L_1} = \frac{1}{\omega_0^2 L_1 k^2}. \end{aligned} \tag{A.10}$$

Assuming the coupling coefficient k is small, i.e. $k^2 \ll 1$, the inductance $(1-k^2)L_1$ can be approximated as L_1. At resonance, the capacitance C_1 cancels L_1 and $k^2 L_1$ cancels C_ref. Thus, at resonance, the circuit in Fig. A.9 simplifies to the circuit shown in Fig. A.10. The efficiency of transferring power from the power generator to the reflected secondary side is

$$\eta_\mathrm{ref} = \frac{P_\mathrm{ref}}{P_\mathrm{tot}} = \frac{R_\mathrm{ref} i_1^2}{(R_1 + R_\mathrm{ref}) i_1^2} = \frac{R_\mathrm{ref}}{R_1 + R_\mathrm{ref}}. \tag{A.11}$$

Similarly, the efficiency of dissipating power in the load can be expressed as

$$\eta_L = \frac{R_\mathrm{L}}{\frac{1}{R_\mathrm{p2}} + \frac{1}{R_\mathrm{L}}} = \frac{R_\mathrm{p2}}{R_\mathrm{p2} + R_\mathrm{L}}. \tag{A.12}$$

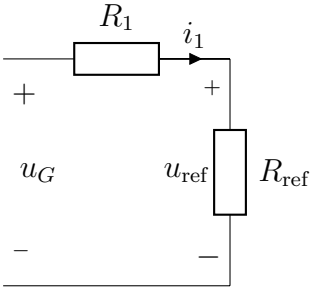

Figure A.10: Equivalent circuit at resonance.

Thus, the total efficiency of the two-coil transmission system is

$$\eta = \frac{R_{\text{ref}}}{R_1 + R_{\text{ref}}} \frac{R_{\text{p2}}}{R_{\text{p2}} + R_{\text{L}}}.$$

We define the load quality factor as $Q_{\text{L}} = \frac{R_{\text{L}}}{\omega_0 L_2}$ and use $Q_{2\text{L}}$ from Eq. (A.9) to express the efficiency as

$$\begin{aligned}
\eta &= \frac{R_{\text{ref}}}{R_1 + R_{\text{ref}}} \frac{R_{\text{p2}}}{R_{\text{p2}} + R_{\text{L}}} = \frac{k^2 \omega_0 L_1 Q_{2\text{L}}}{k^2 \omega_0 L_1 Q_{2\text{L}} + R_1} \frac{Q_2^2 R_2}{Q_2^2 R_2 + R_{\text{L}}} = \\
&= \frac{k^2 \frac{\omega_0 L_1}{R_1} Q_{3L}}{1 + k^2 \frac{\omega_0 L_1}{R_1} Q_{3L}} \frac{Q_2^2 R_2}{Q_2^2 R_2 + R_{\text{L}}} = \left\{ Q_1 = \frac{\omega_0 L_1}{R_1} \right\} = \\
&= \frac{k^2 Q_1 Q_{2\text{L}}}{1 + k^2 Q_1 Q_{2\text{L}}} \frac{Q_2}{Q_2 + \frac{R_{\text{L}}}{Q_2 R_2}} = \{ Q_2 R_2 = \omega_0 L_2 \} = \\
&= \frac{k^2 Q_1 Q_{2\text{L}}}{1 + k^2 Q_1 Q_{2\text{L}}} \frac{Q_2}{Q_2 + \frac{R_{\text{L}}}{\omega_0 L_2}} = \left\{ Q_{\text{L}} = \frac{R_{\text{L}}}{\omega_0 L_2} \right\} = \\
&= \frac{k^2 Q_1 Q_{2\text{L}}}{1 + k^2 Q_1 Q_{2\text{L}}} \frac{Q_2}{Q_2 + Q_{\text{L}}}
\end{aligned} \tag{A.13}$$

Note that the load quality factor Q_{L} and the loaded quality factor $Q_{2\text{L}}$ are quality factors of parallel resonators, while Q_1 and Q_2 are the quality factors of series resonator.

The derivation of the efficiency relies on two approximations: (i) both the primary and the secondary circuit resonates at the same frequency, i.e. $\omega_0 = 1/\sqrt{L_1 C_1} = 1/\sqrt{L_2 C_2}$; and (ii) the coupling coefficient is small, i.e. $k^2 \ll 1$.

An optimal load quality factor can be found by differenting (A.13) with respect to (wrt.) Q_{L}. First, we write η as

$$\begin{aligned}
\eta(Q_{\text{L}}) &= \frac{k^2 Q_1 Q_{2\text{L}}}{1 + k^2 Q_1 Q_{2\text{L}}} \frac{Q_2}{Q_2 + Q_{\text{L}}} = \frac{k^2 Q_1}{\frac{1}{Q_{2\text{L}}} + k^2 Q_1} \frac{Q_2}{Q_2 + Q_{\text{L}}} = \left\{ Q_{2\text{L}} = \frac{Q_2 Q_{\text{L}}}{Q_2 + Q_{\text{L}}} \right\} = \\
&= \frac{k^2 Q_1}{k^2 Q_1 + \frac{1}{Q_2} + \frac{1}{Q_{\text{L}}}} \frac{Q_2}{Q_2 + Q_{\text{L}}} = \frac{k^2 Q_1 Q_2}{k^2 Q_1 Q_2 + k^2 Q_1 Q_{\text{L}} + 2 + \frac{Q_2}{Q_{\text{L}}} + \frac{Q_{\text{L}}}{Q_2}}.
\end{aligned}$$

Differentiation of η wrt. Q_L yields

$$\frac{d\eta}{dQ_\mathrm{L}} = -\frac{k^2 Q_1 Q_2 \left(k^2 Q_1 - \frac{Q_2}{Q_\mathrm{L}^2} + \frac{1}{Q_2}\right)}{\left(k^2 Q_1 Q_2 + k^2 Q_1 Q_\mathrm{L} + 2 + \frac{Q_2}{Q_\mathrm{L}} + \frac{Q_\mathrm{L}}{Q_2}\right)^2}.$$

This maximizes when $k^2 Q_1 - \frac{Q_2}{Q_\mathrm{L}^2} + \frac{1}{Q_2} = 0$, which gives the optimal load quality factor $Q_\mathrm{L}^\mathrm{opt}$ as

$$Q_\mathrm{L}^\mathrm{opt} = \pm\sqrt{\frac{Q_2^2}{1 + k^2 Q_1 Q_2}}. \tag{A.14}$$

The quality factor is a positive number and, thus, we can discard one solution in Eq. (A.14). Thus, the optimal load quality factor is

$$Q_\mathrm{L}^\mathrm{opt} = \frac{Q_2}{\sqrt{1 + k^2 Q_1 Q_2}}. \tag{A.15}$$

This gives us the optimal load resistance as

$$R_\mathrm{L}^\mathrm{opt} = \frac{\omega_0 L_2 Q_2}{\sqrt{1 + k^2 Q_1 Q_2}} = R_2 \frac{Q_2^2}{\sqrt{1 + k^2 Q_1 Q_2}} \tag{A.16}$$

From Eq. (A.13), it follows that the transfer efficiency maximizes for large Q_1, Q_2 and k and optimal efficiency is achieved for the load resistance given in Eq. (A.16).

If we insert Eq. (A.15) into Eq. (A.13), we find the optimal efficiency as

$$\eta^\mathrm{opt} = \frac{1}{1 + \frac{2}{k^2 Q_1 Q_2}\left(1 + \sqrt{1 + k^2 Q_1 Q_2}\right)}. \tag{A.17}$$

The optimal efficiency expressed in Eq. (A.17) increases monotonically with k. If we assume that the quality factors are equal, i.e. $Q_1 = Q_2 = Q$, we can express Eq. (A.17) in terms of the dimensionless quantity kQ, i.e.

$$\eta^\mathrm{opt} = \frac{1}{1 + \frac{2}{(kQ)^2}\left(1 + \sqrt{1 + (kQ)^2}\right)}. \tag{A.18}$$

In Fig. A.11, we plot the optimal efficiency as a function of kQ. It is clearly visible in Fig. A.11 that the transfer efficiency rapidly increases with kQ. Given that $k \approx 0.1$ and $Q \approx 1000$ for a typical wireless energy transfer system in this thesis, we can conclude that the optimal efficiency is close to unity.

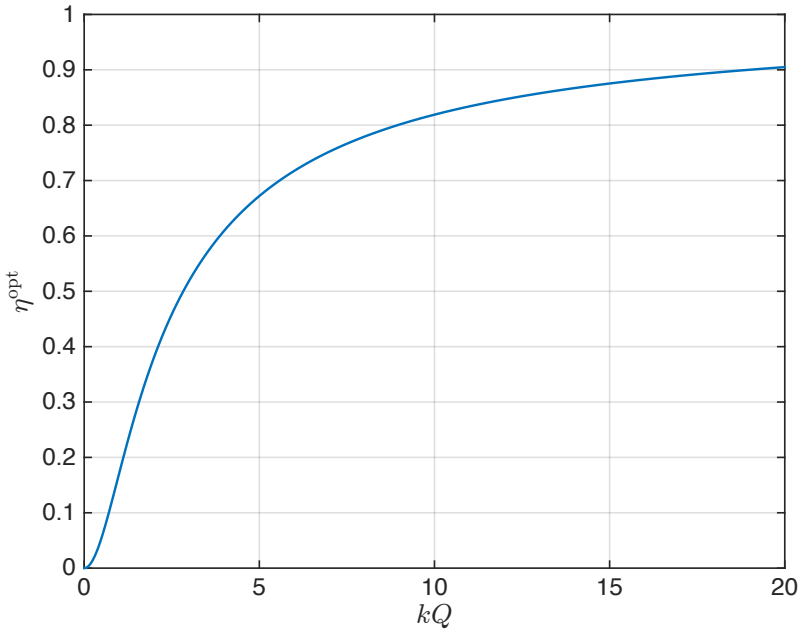

Figure A.11: The optimal transfer efficiency as a function of the quantity kQ.

B

Numerical modelling for the field problem

In this appendix, we compare the results of the COMSOL models with analytical calculations to verify the correctness of the FEM models. Further, we extrapolate the FEM models to zero cell-size and study the error of the solutions for finite cell-size.

B.1 Validation of the COMSOL model

This section compares the quantities calculated in the FEM model with the analytic formulas.

First, a single wire loop of radius 0.3 m is excited by 1 A and the magnetic field is calculated along the symmetry axis. Fig. B.1 presents from the analytical result and the corresponding graph based on FEM computations. The magnetic field is

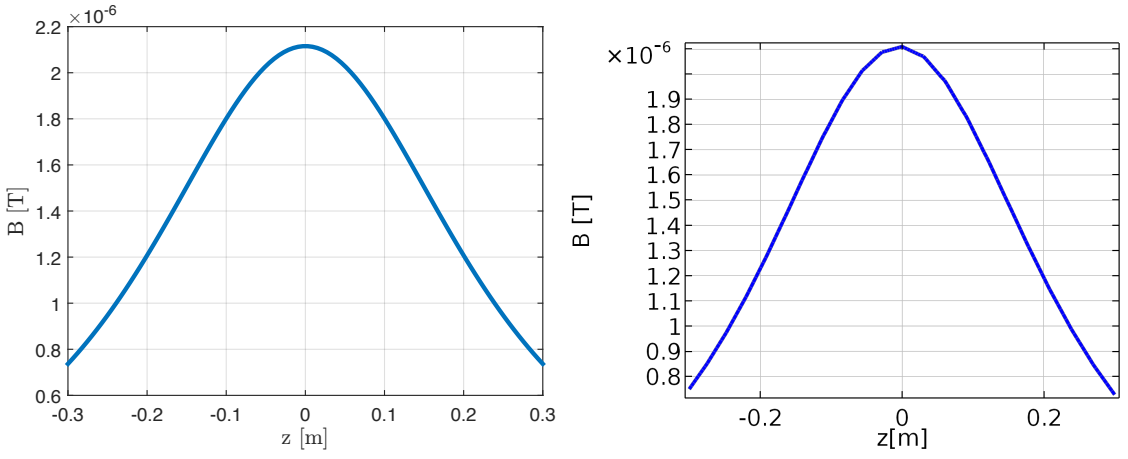

(a) **(b)**

Figure B.1: Analytic (a) and FEM (b) calculations of the magnetic field along the symmetry axis for a single wire loop of radius 0.3 m excited by 1 A.

essentially identical in the two graphs. To verify the "multi-turn coil domain" in

COMSOL, we consider a similar situation with a coil with $N_r = 4$ and $N_z = 2$ turns. The outer radius is still 0.3 m and the distance between the windings is 7 mm. The magnetic field along the symmetry axis is shown in Fig. B.2. Once again, the COMSOL

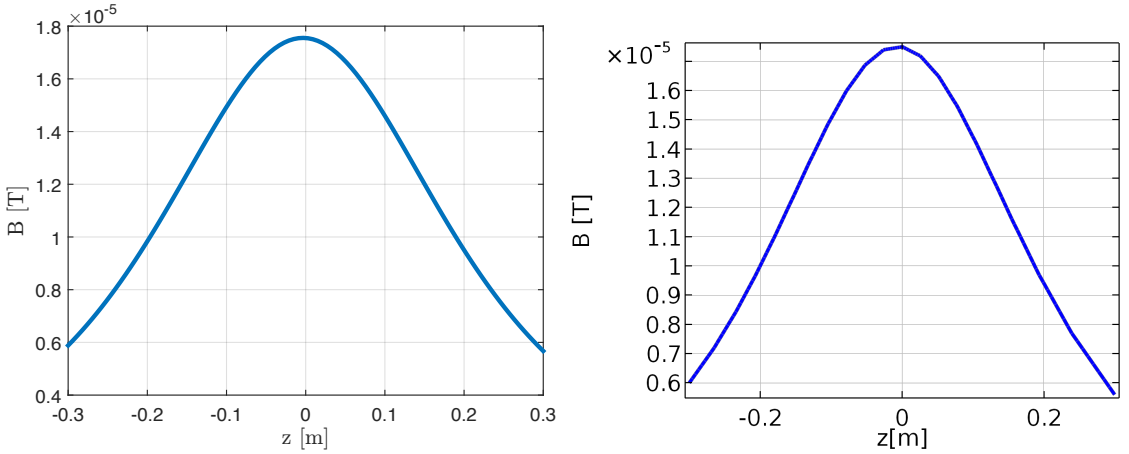

(a) **(b)**

Figure B.2: Analytic (a) and FEM (b) calculations of the magnetic field along the symmetry axis for a coil with $N_r = 4$ and $N_z = 2$ and outer radius 0.3 m excited by 1 A. The distance between wire loops is 7 mm.

model yields the same magnetic field as the analytic expression. Thus, the multi-turn coil domain can correctly compute the magnetic field along the symmetry axis for coils with multiple windings.

The analytical expression for the magnetic flux linkage between two conducting loops, based on elliptic integrals, assumes that the cross section of the wires is small compared to the other dimensions of the system. As the wires in COMSOL cannot be infinitely small, we perform a convergence study where the radius of the wires in the two coils are gradually decreased. Figure B.3 shows the error

$$\varepsilon = \frac{|M_{\text{COMSOL}} - M_{\text{Analytic}}|}{M_{\text{Analytic}}}$$

as a function of the wire radius. The FEM calculations converge toward the analytic solution with an order of convergence of one.

The self- and mutual inductance of the multi-turn coil is calculated analytically using Eq. (2.15) and compared to the FEM calculations in Tab. B.1. To test the circuit model with the FEM solver, the inductances and resistances found in Tab. B.1 is inserted into the circuit in Fig. 2.1. The capacitances is chosen such that $L_1C_1 = L_2C_2$ and the generator voltage and resistance is set to 220 V and 1 Ω, respectively. The load resistance is chosen according to Eq. (2.19). The circuit problem is solved and the coil currents computed by the circuit solver are used in the FEM solver. This gives the total field solution as the coils are driven by the external circuitry. The voltage over the coil calculated using the circuit model and the FEM solver is shown in Tab. B.2.

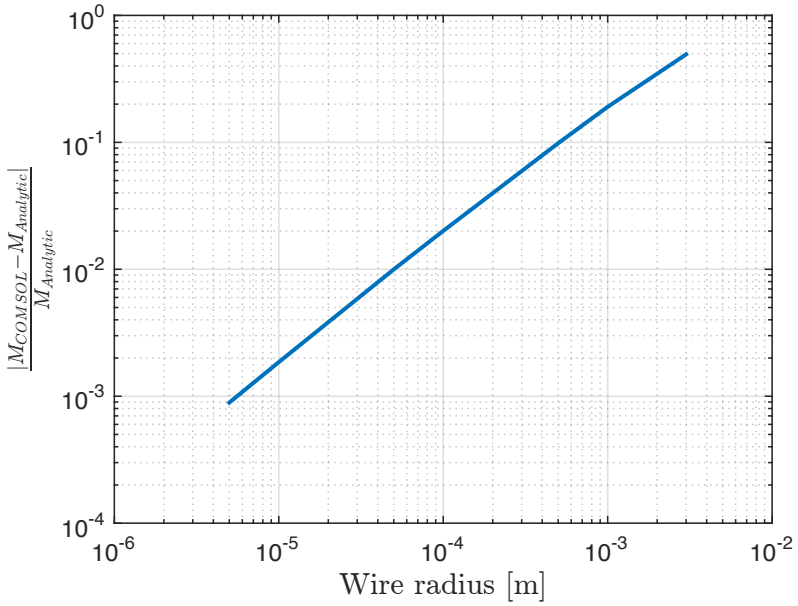

Figure B.3: Convergence of the FEM computations toward the analytical mutual inductance for two coaxial, single loop coils, one of radius 0.3 m and one of radius 0.01 m, located 0.1 m apart. The quantity on the x-axis is the wire radius of both coils.

Table B.1: Self- and mutual inductance and resistance calculated analytically and in COMSOL of two identical, coaxial coils of $N_\mathrm{r} = 4$, $N_\mathrm{z} = 2$, wire radius 3 mm and loop distance 7 mm. The coils are displaced 0.3 m from each other. A litz wire density of 0.9 is assumed.

	Analytic	COMSOL
Self-inductance	81.490 μH	81.491 μH
Mutual inductance	7.9324 μH	7.9327 μH
Resistance	10.68 mΩ	10.84 mΩ

Table B.2: Voltage over coils calculated using the circuit model and the FEM solver.

	Circuit	COMSOL
V_coil1	$35.91 + i1813$ V	$35.89 + i1812$ V
V_coil2	$1814 + i122.8$ V	$1813 + i122.7$ V

To conclude, the magnetic field, magnetic flux, induced voltage, inductance and resistance calculated using COMSOL are all in accordance with the analytical expressions.

B.2 Extrapolation, accuracy and convergence of the numerical model

In computational electromagnetics, the problems that have analytical solutions is limited. Often, the problems are instead solved using numerical techniques such as the FEM. In this project, the basis functions are second-order polynomials on triangular finite elements. The accuracy of the models are studied by means of convergence tests, where the field problem is solved for a set of adaptively refined meshes. From these consecutive computations, an estimate of the exact solution can be found by extrapolation.

The aim of this chapter is to get a feeling for how many adaptive mesh refinements are needed to achieve a certain degree of accuracy. The convergence is studied for one single problem geometry and the results can, therefore, only be used as an estimate of the accuracy for other geometries. However, it can be assumed that the same number of adaptive mesh refinements yields similar accuracy for other geometries.

B.2.1 Adaptive mesh refinement

The straightforward method of refining a triangular mesh is simply dividing each element into two, or more, elements. However, the number of elements grows exponentially with this procedure. A different approach is to use adaptive mesh refinement [15]. Then, the problem is solved once with an unrefined mesh, which gives information about what parts of the mesh that contribute most to the error. These regions typically feature rapid field variations. By studying the solution from the unrefined mesh and refining only the regions with large error estimates, the number of additional elements can be decreased while the accuracy is increased.

The geometry of the two-coil system studied in this project contains both sharp corners, where singularities are highly probable, and objects of drastically different physical size, e.g. the ferrite core size and coil wire radius. Therefore, the adaptive refinement scheme is useful to achieve high accuracy, while the number of elements is kept low.

B.2.2 Extrapolation

From a circuit theory point of view, the interesting results are the resistance, self-inductance, mutual inductance and quality factor of the two coils in the system. To understand the convergence of these properties the simulated results are compared to a simple, first-order expansion model. In the following, we use the resistance as an example, but the other quantities can be treated similarly. In the case of coil resistance, the model is

$$R_{\text{model}}(N_{\text{DOF}}) = R_0 + R_\alpha N_{\text{DOF}}^\alpha, \tag{B.1}$$

where N_{DOF} is the number of degrees of freedom for the particular mesh, α the estimated order of convergence, R_0 the extrapolated solution and $R_\alpha N_{\text{DOF}}^\alpha$ is the leading error.. Note that similar first-order models can be constructed for the self- and mutual inductance and any other property of interest. By performing N_{refine} refinements one can construct the matrix

$$\mathbf{A} = \begin{bmatrix} 1 & N_{\text{DOF},1}^\alpha \\ 1 & N_{\text{DOF},2}^\alpha \\ \vdots & \\ 1 & N_{\text{DOF},N_{\text{refine}}}^\alpha \end{bmatrix},$$

and the matrix equation

$$\mathbf{A}\mathbf{x} = \mathbf{R}_{\text{sim}},$$

where $\mathbf{x} = [R_0 \ R_\alpha]^{\text{T}}$ and $\mathbf{R}_{\text{sim}}$ is the simulated resistances. This is typically an overdetermined equation system where $N_{\text{refine}} > 2$ and it can either be solved by linear least-square methods or by constructing the square matrix $\mathbf{A}^{\text{T}}\mathbf{A}$ and solve the system by inversion

$$\begin{aligned} \mathbf{A}\mathbf{x} &= \mathbf{R}_{\text{sim}}, \\ \mathbf{A}^{\text{T}}\mathbf{A}\mathbf{x} &= \mathbf{A}^{\text{T}}\mathbf{R}_{\text{sim}}, \\ \mathbf{x} &= \left(\mathbf{A}^{\text{T}}\mathbf{A}\mathbf{x}\right)^{-1}\mathbf{A}^{\text{T}}\mathbf{R}_{\text{sim}}. \end{aligned}$$

The residual is computed as

$$r(\alpha) = ||\mathbf{A}\mathbf{x} - \mathbf{R}_{\text{sim}}|| = \left|\left|\left(\mathbf{A}\left(\mathbf{A}^{\text{T}}\mathbf{A}\mathbf{x}\right)^{-1}\mathbf{A}^{\text{T}} - \mathbf{I}\right)\mathbf{R}_{\text{sim}}\right|\right|.$$

where $||\mathbf{A}||$ is the 2-norm of $\mathbf{A}$. The found R_0 is assumed to be an accurate estimate of the exact solution. The problem is then to find the value of α which minimizes the residual r. The optimal α is found by sweeping the parameter, calculating $r(\alpha)$ for each value and selecting the α which yields the smallest r.

A common problem is that the matrix $\mathbf{A}$ becomes ill-conditioned, i.e. there are several orders of magnitude between the largest and smallest element in the matrix. For $N_{\text{DOF}} = 10^6$ and $\alpha = -3$, a not unreasonable situation, the matrix $\mathbf{A}$ contain values between 1 and 10^{-18}, which results in an ill-conditioned problem.

One solution is to scale the columns by the median value of N_{DOF}. The typical number of degrees of freedom is defined as $N_{\text{typ}} = \text{median}\left\{N_{\text{DOF},1}, N_{\text{DOF},2}, \ldots, N_{\text{DOF},N_{\text{refine}}}\right\}$ and we formulate the new matrix

$$\mathbf{A}' = \begin{bmatrix} 1 & \left(\frac{N_{\text{DOF},1}}{N_{\text{typ}}}\right)^\alpha \\ 1 & \left(\frac{N_{\text{DOF},2}}{N_{\text{typ}}}\right)^\alpha \\ \vdots & \\ 1 & 1 \\ \vdots & \\ 1 & \left(\frac{N_{\text{DOF},N_{\text{refine}}}}{N_{\text{typ}}}\right)^\alpha \end{bmatrix}.$$

Note that the row where $N_{\mathrm{DOF}} = N_{\mathrm{typ}}$ contains only ones. The second column of the matrix is now centered around and closer to one than before. The matrix equation then becomes

$$\mathbf{A}'\mathbf{x}' = \mathbf{R}_{\mathrm{sim}},$$

where $\mathbf{x} = [R_0 \; R'_\alpha]^{\mathrm{T}}$ and $R_\alpha = R'_\alpha / N^\alpha_{\mathrm{typ}}$.

Observe that N_{typ} can be chosen by other methods depending on the values of N_{DOF}. Other choices are the arithmetic or geometric mean value of N_{DOF}.

B.2.3 Accuracy of the model

The error between the model $R(N_{\mathrm{DOF}})$ and the extrapolated resistance R_0 in Eq. (B.1) can be estimated as

$$e = R(N_{\mathrm{DOF}}) - R_0. \tag{B.2}$$

In reality, the resistance of a manufactured coil differs from the extrapolated R_0. In the following, we denote the resistance of a manufactured coil $\tilde{R}_0$. The error between the model $R(N_{\mathrm{DOF}})$ and $\tilde{R}_0$ is

$$\tilde{e} = R(N_{\mathrm{DOF}}) - \tilde{R}_0 = R(N_{\mathrm{DOF}}) - R_0 + R_0 - \tilde{R}_0 = e + R_0 - \tilde{R}_0.$$

The error $e \to R_0$ as $N_{\mathrm{DOF}} \to \infty$. However, the error $\tilde{e}$ does not tend to zero due to the constant factor $R_0 - \tilde{R}_0$. This factor constitutes all errors that are not included in the extrapolated result R_0. Such error sources are the real coil being constructed from one continuous wire instead of several coaxial loops, uncertainties in the manufacturing of the coils, ferrite plates, metal plates, the real problem is not rotationally symmetric, etc. In a typical engineering setting, it is acceptable if these errors are on the order of percent.

The gradient calculations uses the difference between two slightly different problems to calculate the derivatives. If the error in the individual simulations is too large, the gradient is prone to be uncertain. Thus, the error in the simulations must have higher accuracy than the wanted accuracy in the gradient computations. A simulation accuracy of 0.1% is deemed high enough.

B.2.4 Convergence study

To identify the number of adaptive mesh refinements necessary to achieve 0.1% accuracy, a representative geometry is selected for testing and several consecutive adaptive mesh refinements are carried out. In Fig. B.4 the resistance and inductance of one of the two coils is shown as a function of the number of degrees of freedom. In all cases, the computed quantity is well within the sought-after 0.1% accuracy after one adaptive mesh refinement. The order of convergence is presented in Tab. B.3. The achieved convergence is slow but the initial accuracy is high enough to ensure that the first adaptive refinement is well within the 0.1% accuracy.

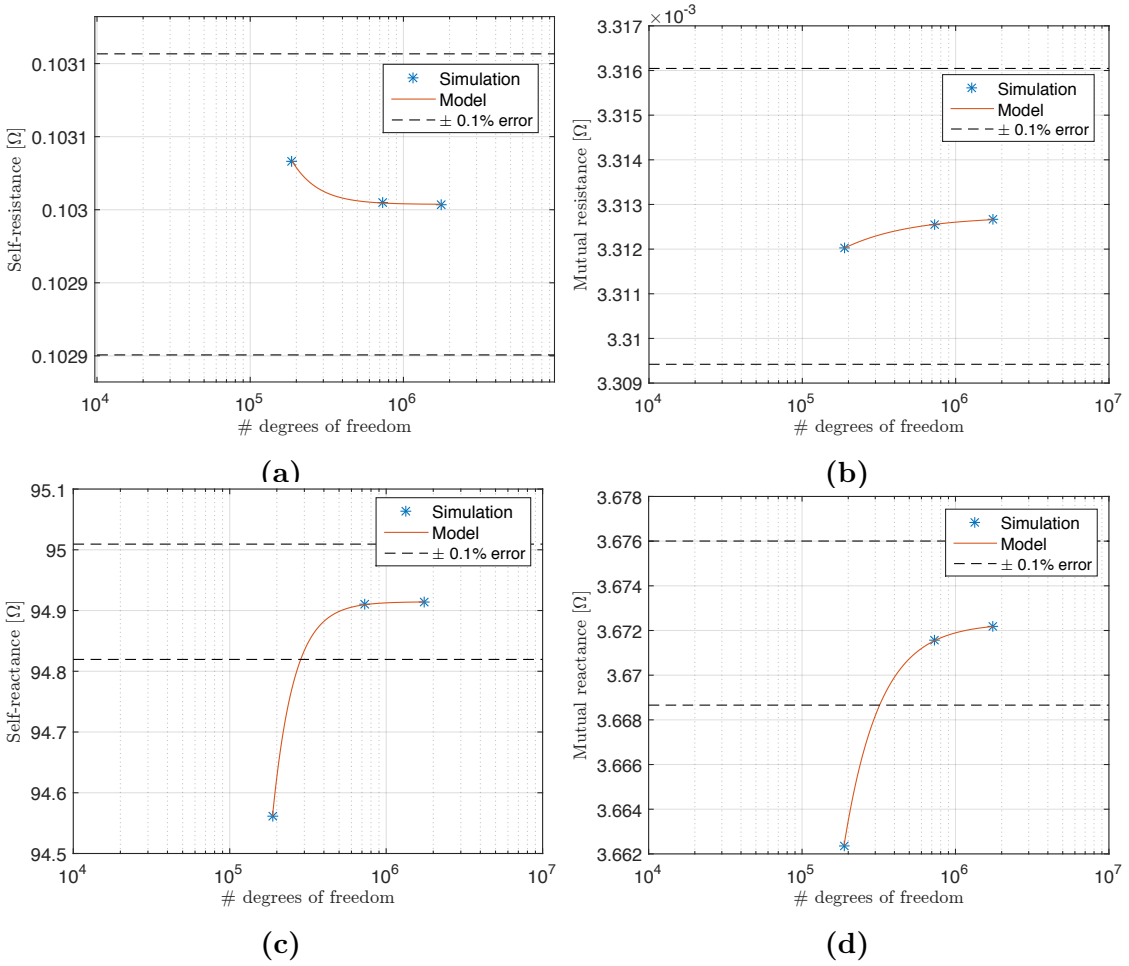

Figure B.4: Convergence in (a) self-resistance, (b) mutual resistance, (c) self-inductance and (d) mutual inductance. The dashed lines indicate levels of ±0.1% error and they are calculated from the extrapolated value.

Table B.3: Order of convergence for the coil resistance and inductance.

	Order of convergence
Self-resistance	-2.5
Mutual resistance	-1.0
Self-inductance	-3.2
Mutual inductance	-1.9